CHINESE OPTICS LETTERS | Fast Track

Vol. 21, No. 6 | June 2023

# Quasiperiodic photonic crystal fiber [Invited]

Exian Liu (刘娥贤)[1] and Jianjun Liu (刘建军)[2*]

[1] College of Computer and Information Engineering, Central South University of Forestry and Technology, Changsha 410004, China

[2] Key Laboratory for Micro/Nano Optoelectronic Devices of Ministry of Education & Hunan Provincial Key Laboratory of Low-Dimensional Structural Physics and Devices, School of Physics and Electronics, Hunan University, Changsha 410082, China

*Corresponding author: jianjun.liu@hnu.edu.cn

Received March 24, 2023 | Accepted March 29, 2023 | Posted Online May 3, 2023

In the fields of light manipulation and localization, quasiperiodic photonic crystals, or photonic quasicrystals (PQs), are causing an upsurge in research because of their rotational symmetry and long-range orientation of transverse lattice arrays, as they lack translational symmetry. It allows for the optimization of well-established light propagation properties and has introduced new guiding features. Therefore, as a class, quasiperiodic photonic crystal fibers, or photonic quasicrystal fibers (PQFs), are considered to add flexibility and richness to the optical properties of fibers and are expected to offer significant potential applications to optical fiber fields. In this review, the fundamental concept, working mechanisms, and invention history of PQFs are explained. Recent progress in optical property improvement and its novel applications in fields such as dispersion control, polarization-maintenance, supercontinuum generation, orbital angular momentum transmission, plasmon-based sensors and filters, and high nonlinearity and topological mode transmission, are then reviewed in detail. Bandgap-type air-guiding PQFs supporting low attenuation propagation and regulation of photonic density states of quasiperiodic cladding and in which light guidance is achieved by coherent Bragg scattering are also summarized. Finally, current challenges encountered in the guiding mechanisms and practical preparation techniques, as well as the prospects and research trends of PQFs, are also presented.

**Keywords:** photonic quasicrystal fiber; guiding mechanism; guiding features and applications; challenges and prospects.
**DOI:** 10.3788/COL202321.060603

## 1. Introduction

In early 1984, the discovery of quasiperiodic crystals (also called quasicrystals) in aluminum–magnesium alloys, achieved by Shechtman and his co-workers, led to the formation of a new type of solid different from the other well-known amorphous and periodic crystals based on basic atomic or molecular structures[1]. The two-dimensional (2D) diffraction pattern of this quasicrystal was found to present a long-range order feature (but with no periodicity), fully countering the law of the existing ordered crystal, and was demonstrated to match Penrose and Mackay's mathematical model in which a mosaic could be laid with a few rhombic tiles[2–4]. Figures 1(a) and 1(b) show the common five-fold Penrose lattice tiling and the corresponding numeric diffraction pattern[5]. By utilizing the cut-and-project method[6], the projection (. . . ABAABA . . . ) of the regular stripe of the 2D quasiperiodic lattice on the virtual curve with an irrational slope is generated endlessly, which perfectly matches the 1D Fibonacci lattice [Fig. 1(c)][5]. Several years later, dodecagonal quasicrystals were found in solidified $V_3Ni_2$ and $V_{15}Ni_{10}Si$ alloys and showed a quasiperiodic pattern consisting of squares and equilateral triangles, basically consistent with Stampfli's model[6,7]. The unique quasiperiodic arrangement and geometry of the constituent unit then inspired intense explorations in the fields of chemistry, material science, mathematics, and in particular, optics[8–15].

Around 1998, a 2D quasicrystal arrangement of dielectrics [photonic quasicrystal, (PQ)] was first introduced in the optical field[16] after intensive studies on the optical, electrical, and acoustic properties[17] of 1D quasicrystals (such as the Fibonnaci sequence superlattice[18]). These studies showed significant breakthroughs regarding the features of the photonic bandgap (PBG), such as having more flexibility in tuning the defect state properties and having extremely large wavelengths[19–22]. For instance, a twelve-fold symmetric PQ can enable the realization of complete non-directional PBGs for backgrounds with lower refractive indices, even for silica material[23]. The scanning electron microscopy (SEM) images of a twelve-fold symmetric PQ and the multiple diffracted beams from the entrance face are presented in Figs. 1(d) and 1(e), respectively.

In the following twenty years, tremendous research efforts had been devoted to studying the interesting optical physics of PQs (including photonic dispersion relation, plasmonic,

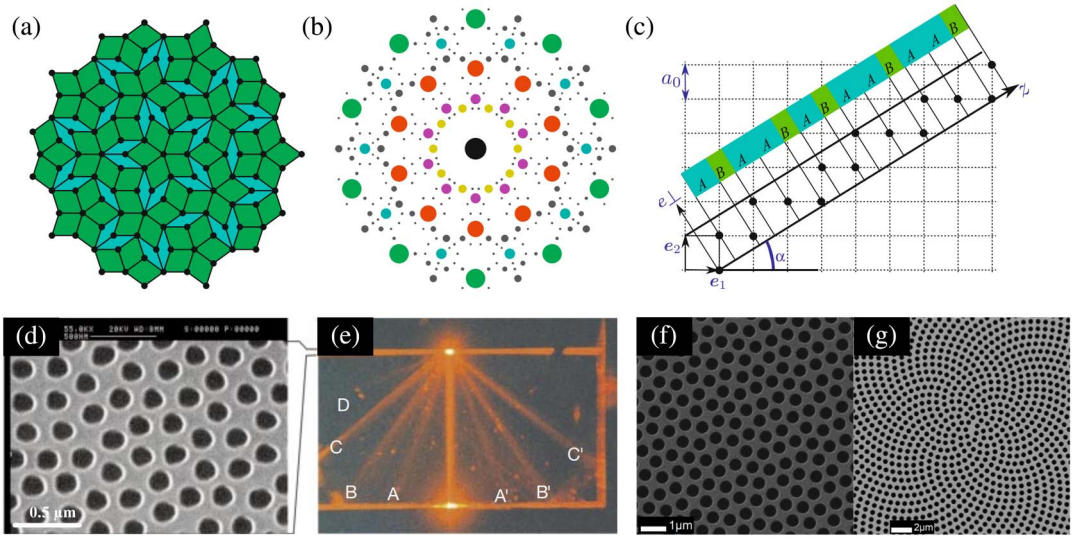


**Fig. 1.** (a) Five-fold Penrose lattice tiling pattern[5]. (b) Diffraction pattern of the five-fold Penrose-type PQ structure[5]. (c) 1D Fibonacci sequence generated by the 2D PQ lattice using the cut-and-project method[5]. (d) Fabricated silica-based twelve-fold symmetric quasicrystals[23]. (e) Multiple diffracted beams from the entrance face of the twelve-fold symmetric quasicrystals[23]. (f) and (g) Fabricated Si-based twelve-fold PQ and Sunflower-type PQ structures by E-beam lithography system[64].

complete PBG, localized states, optical transmission, light transport, etc.) for device applications in super-resolution lenses, lasers, sensors, topological photonics, meta-surfaces, and fibers[24–56]. Moreover, the interdisciplinary applications have also attracted significant research interest, with the PQ concept introduced in other scientific fields[11–15,57–63]. Interestingly, research conducted in 2021 showed that surface texturing etched with a PQ array pattern could significantly reduce surface reflection loss, which is the key for creating next-generation high-efficiency Si solar cells[64]. The involved Stampfli-type PQ and Sunflower-type PQ patterns are shown in Figs. 1(f) and 1(g).

The modern optical fiber, one of the most successful technological inventions of the 20th century, has become indispensable to current global long-distance telecommunication networks and non-telecommunication applications involving light transportation, such as diagnostics, medicine, laser, imaging, sensing, and probes. For non-telecom fibers or specific fibers[65], the microstructure fiber on the scale of the optical wavelength, such as the typical photonic crystal fiber (PCF), has been demonstrated to have high superiority in light guidance with a host of characteristics as compared with the traditional step-index fiber. This has promoted the renaissance of research interest in optical fibers in the latter 40 years of the 20th century[66]. This originates from the periodic-lattice structure of the cladding and a large index contrast, which enables richer ways to improve optical properties. Moreover, the existence of a complete PBG in the region of the propagation constant $\beta < k$ wavelength vector, where light can propagate freely in the vacuum, offers the possibilities of extending the guiding mechanism of fibers from the total internal reflection to the PBG effect. In nature, manipulating light in the PCF involves engineering a cladding structure on the cross-sectional plane because the PCF approximates 2D structures due to its infinity in another dimension[67]. This indicates that the introduction of the quasi-periodic dielectric structure, which features new characteristics of photonic bands in the optical fiber, provides additional opportunities to manage the fiber properties.

The properties of light propagation in the PQ are governed by the photonic dispersion relation. Although no strict Brillouin zone exists in the reciprocal space of the PQ, it is still possible to construct the "effective Brillouin zone" by calculating the "pseudo-Jones" zone with a description of a set of relatively intense reciprocal vectors[37]. Owing to the long-range order and self-similarity of the 2D PQ structure, the dispersion relation exhibits a richness, uniqueness, and flexibility with a well-designed structure. Therefore, both the realization of the PCF and the proposal of the PQ concept stimulate the development of the PQF, which is illustrated by the PQF evolution diagram shown in Fig. 2.

In 2007, the PQ structure was primarily employed in optical fibers in which transverse air-hole lattices were arranged following the rule of a basic unit or part of a PQ array. Moreover, compared with the PCF, the constructed dodecagonal Stampfli-type PQF exhibited an easily tailed, near-zero flattened dispersion and a larger cutoff ratio for endlessly single-mode operation due to relatively complex and unusual light reflection in the cladding[68]. Note that the PQF still belongs to the class of microstructure fibers and consists of specific quasiperiodic air-hole arrays that differ from the periodic PCF. The local PQ structure introduced in the cladding, cannot be accurately characterized by the full PBGs of the PQ. Nevertheless, high geometric degrees of freedom in PQs, including the air hole size, the lattice constant, and the fold number, outperform the conventional PCF in quite a few aspects.

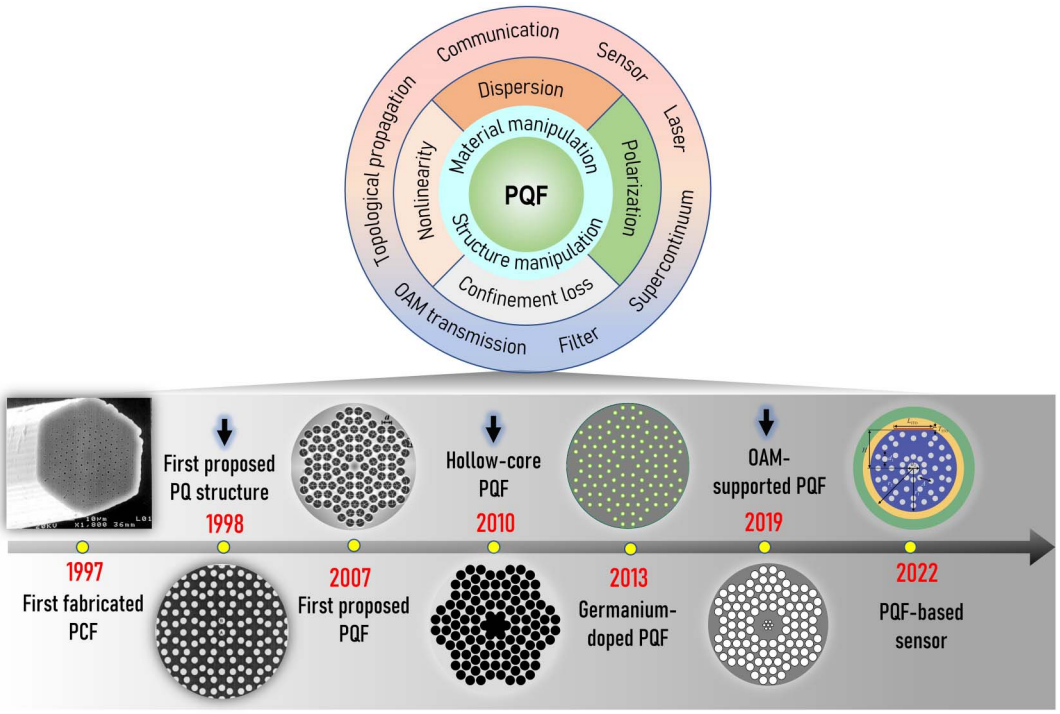


**Fig. 2.** Upper circular diagram showing the potential technological applications with the optical properties optimized using the structure and material manipulation based on a PQF. The bottom arrow indicates the PQF evolution from the first fabricated PCF[67] to the first reported PQ structure[16], to the first proposed PQF[68], to the hollow-core PQF[72], to the Ge-doped PQF[99], to the OAM-supported PQF[95], and to the PQF-based sensor[96].

Accordingly, in the following decade, outstanding or interesting guiding properties of the PQF, such as the opposite dependence of the lattice constant on the negative dispersion[69], the fold number-dependent validity of the $V$ parameter[70], an ultra-high birefringence of $3.86 \times 10^{-2}$[71], a two-guided band in the hollow PQF[72], and the low confinement loss with a well limited mode by means of rotational cladding[73], were reported repeatedly, which further promoted PQF-based device designs of specific fibers, amplifiers, stretchers, sensors, and filters in optical communications and sensor systems[74–94]. Part of the optical properties and applications are shown in Fig. 2, based on material and structure manipulation. Recently, PQFs have been found to well support the orbital angular momentum (OAM) mode due to this mode's perfect mode shape, which matches the circular fiber structure. This design may provide new ideas in mode-division multiplexing for satisfying the surge in telecommunication data[95–98]. Moreover, for guiding fibers at the infrared and terahertz wavelengths, in the topologically protected mode transmission, and in fiber-based devices of lasers and metalenses, the PQF is expected to be a promising candidate platform.

In summary, specific rotational symmetry and long-range orientation of transverse lattice arrays found in PCFs, which lack translational symmetry, endow PQFs with more structural degrees of freedom and unique cladding arrangements that offer more flexibility in tuning guiding features for specific applications.

## 2. Light-Guiding Mechanism in the PQF

As mentioned in Section 1, the air-hole arrangement in the cladding determines the PBG in the transverse section and further changes the effective index difference between the cladding and the core of fiber, which shapes the propagation properties of the guiding modes. Three types of PQFs are first introduced in this section, and then the guiding mechanisms in the solid-core PQF and the hollow-core PQF are briefly discussed.

### 2.1. Classification of PQFs

According to the characteristics of the PQF, which features a rotational symmetry and no transmission periodicity, the PQF can be divided into the following three categories: the Stampfli-type PQF, the Penrose-type PQF, and the Sunflower-type PQF. In general, only part of the rotational air-hole arrays of the PQ (such as the first- or second-order unit) are introduced in the cladding of the fiber. However, the unique fiber structure definitely exhibits interesting properties when compared with the conventional PCF.

#### 2.1.1. Stampfli-type PQF

In the Stampfli-type PQF, the basic rotational unit is composed of two adjacent polygons: one square (interior angle $\pi/2$) and the other an equilateral triangle (interior angle $\pi/3$). By rotating these adjacent polygons six times around the center,

the first-order unit can be obtained, as shown in Fig. 3(a). Considering the first-order unit as a point, the second-order unit can be obtained following the same matching rule in a similar fashion [see Fig. 3(b)]. Then, it is easy to obtain an entire pattern of the PQ, which exhibits high similarity due to a number of basic units. Another PQ pattern can be formed by rotating the basic units with a $\pi/6$ angle, as shown in Fig. 3(c).

#### 2.1.2. Penrose-type PQF

Similar to the Stampfli-type PQF, the basic rotational unit in this type of PQF also includes two or more types of rhombi whose interior angles are determined by the symmetric number. For instance, the interior angles of two rhombi in the eight-fold Penrose-type are $\pi/2$ and $\pi/4$. The groups $\pi/5$, $2\pi/5$ and $\pi/6$, $\pi/3$, $\pi/2$ are for ten-fold and twelve-fold PQFs, respectively. Three diagrams of a transverse section of the fiber are illustrated in Figs. 3(d)–3(f).

#### 2.1.3. Sunflower-type PQF

In addition to the common Stampfli-type and Penrose-type PQFs, the Sunflower-type PQF (also denoted as a circular PCF) fiber has rotational symmetry and no translational symmetry and can also be generally considered as a group. This typical type of fiber contains circular periodic hole arrays other than translational periodicity. Astonishingly, higher structure degrees of freedom exist in this fiber with different numbers of first-ring holes or central angles $\theta$ between two adjacent air holes.

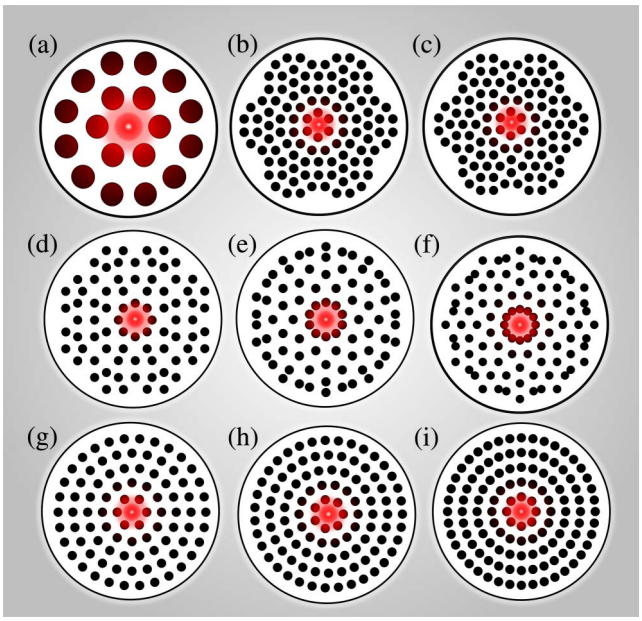


**Fig. 3.** The upper row shows the Stampfli-type PQF. (a) The first-order PQF, (b) the second-order PQF, and (c) the second-order PQF with a $\pi/6$ rotation of the near-core ring of the air holes. The middle row shows the Penrose-type PQF. (d) The eight-fold PQF, (e) the ten-fold PQF, and (f) the twelve-fold PQF. The bottom row shows the Sunflower-type PQF. (g) The six-fold PQF, (h) the seven-fold PQF, and (i) the eight-fold PQF.

Assuming the center of the fiber as the origin in $x$–$y$ plane, the position of each air hole is defined as[90]

$$x = aM\cos\left(\frac{2n\pi}{MN}\right), \tag{1}$$

$$y = aM\sin\left(\frac{2n\pi}{MN}\right), \tag{2}$$

where $a$, $M$, and $n$ represent the lattice constant, the ordinal number of rings, and the integer from 1 to $M \times N$, respectively. $N$ is the number of air holes in the first ring and represents the rotational symmetry. The central angle $\theta$ is given by $\theta = (360/M) \times N$ and shows the angular spacing between any two neighboring air holes in a ring. Setting $N$ to be 6, 7, and 8, the cross-sections of the constructed Sunflower-type PQF are shown in Figs. 3(g)–3(i), respectively. The hole arrangement and air-filling fraction influence the average refractive index. This is the origin of high-performance adjustability for high numerical aperture (NA), dispersion, confinement loss, etc. Note that in order to avoid air hole collapse during fiber preparation, the maximum air hole size for each type of PQFs has to be limited in a certain range, which was partly demonstrated in the previous study[85].

### 2.2. Light-guiding mechanisms of PQFs

Currently, the guiding mechanisms of the reported PQFs can be classified into two categories: the total reflection mechanism (or index-guiding mechanism) and the PBG mechanism (or air-guiding mechanism), which depend on the refractive indices of the core and cladding materials. The two mechanisms correspond to the solid-core PQF and the hollow-core PQF, respectively.

#### 2.2.1. Index-guiding solid-core PQF

For homogeneous medium fibers, the well-known Snell's law is followed at the interface (between the core and cladding). The solid-core PQF exhibits a large-mode index difference between the solid core and the holes containing the cladding arranged by air hole size, which easily introduces a light propagation form of the total internal reflection (TIR) mechanism at a particular frequency[65]. If the PQF is designed with an endlessly single-mode propagation for white light, then all components of the light follow the TIR law, as shown in Fig. 4(a). However, the complex rotational structure and flexible cladding arrangement complicate the mathematical solving process of the mode of the PQF with Maxwell's equations.

#### 2.2.2. Air-guiding hollow-core PQF

In contrast, the well-known hollow-core fiber possesses a lower index of the core than that of the cladding, and the incident light is trapped by the strong reflection in the "stop band" of the photonic band structures of the periodic cladding. Stop bands constrain all the optical vibrations in any direction and limit the

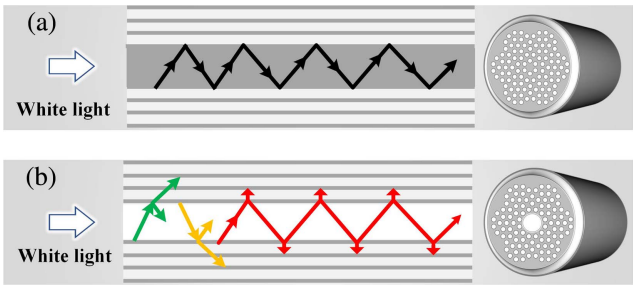


**Fig. 4.** (a) Index-guiding solid-core PQF. (b) The air-guiding hollow-core PQF.

light in the core within all wavelengths spanning the PBG. In this case, the PBGs are functions of the propagation constant $\beta$ rather than those of the optical wavelength. If white light is launched into a fiber core that is designed to work in the red visible region, then only the red component of the light can be guided along the fiber, and other components get attenuated in the cladding, as shown in Fig. 4(b). The guidance existed only in the stop band, coinciding with the PBGs. This indicates that the fiber's periodic structure can shape the mode properties radically, which therefore raises a strict requirement for fiber fabrication technique. The typical PBGs in the PCFs are generated by a wavelength-scale periodic structure. However, the light propagation in the hollow-core PQF is governed by the PBGs generated in the PQ structure. Therefore, the unique photonic band properties of the PQ make it difficult to modulate the mode features of the PQF. For instance, for light guidance, a Stampfli-type hollow-core PQF can offer two PBGs (or low loss windows) in the $\lambda/\Lambda$ region[72], whose feature has not been found in periodic PCF. However, the detailed theoretical explanation about the new light propagation phenomena in the hollow-core PQF needs further clarification and systematic explorations, although such types of fibers have been reported[94].

## 3. Guiding Features and Applications of PQFs

Owing to the quasiperiodic dielectric or air arrays in the cladding region, the photonic dispersion relation is different from that of the PCF, which affects the guiding mode properties, such as distribution and transmission, and accounts for the fold number-dependent validity of the $V$ parameter for clarifying the single-mode and multi-mode operations. Moreover, background material manipulation, together with high structure degrees of freedom, including the air hole size, the lattice constant, and the rotation fold number, enables the PQF to flexibly tail the waveguide dispersion[69], the polarization-maintaining capability[71], the mode-field area[75,99], and the nonlinearity[76]. Moreover, the PQF also provides an excellent structural platform for surface plasmon resonance (SPR)[84], mode coupling[93], and OAM transmission[95]. All these features not only offer opportunities for exploring new complex optical fiber physics but also facilitate the new engineering of fiber devices, including multiplexers, sensors, filters, and amplifiers in the fields of communication, biomedicine, and environmental protection.

### 3.1. Guiding features of PQFs

#### 3.1.1. Single-mode operation and high numerical aperture

The most striking property[67] of the microstructure fiber is the intriguing "endlessly single-mode propagation," featuring a fundamental mode maintained in the core of the arbitrary short wavelength with a proper choice of geometry (air-filling fraction $d/\Lambda$). One parameter that evaluates the quality of the single-mode operation is the cutoff ratio of the air-filling fraction for endless single-mode propagation, since a higher cutoff ratio allows a larger size of the constituent air-hole array of the fiber, making fiber fabrication easier. In general, the $V$ parameter method is used for the evaluation of the cutoff ratio, and the value of the effective $V$ parameter $V_{\mathrm{eff}}(\lambda)$ is calculated as[100]

$$V_{\mathrm{eff}}(\lambda) = \frac{2\pi a}{\lambda}[n^2_{\mathrm{co,eff}}(\lambda) - n^2_{\mathrm{cl,eff}}(\lambda)]^{1/2}, \tag{3}$$

where $n_{\mathrm{co,eff}}(\lambda)$ and $n_{\mathrm{cl,eff}}(\lambda)$ are the effective refractive indices of the core mode and cladding mode, respectively.

In 2003, Mortensen *et al.*[100] proved the cutoff ratio to be 0.406 for the triangular lattice PCF, and Poli *et al.*[101] later accurately obtained the modal cutoff ratio 0.442 in a square-lattice PCF. A comparative analysis of the phase diagram of the second-order mode between the triangular lattice PCF and the square lattice PQF is shown in Fig. 5(a). For the Stampfli-type PQF, Kim *et al.*[68] first reported a cutoff ratio of 0.525 using the $V$ parameter method [Fig. 5(b)], whose value is larger than those of the periodic PCFs. In 2018, it was confirmed that the cutoff ratio for the Sunflower-type PQF could reach the highest value of 0.575 in the previously reported microstructure fibers [Fig. 5(c)][85]. Moreover, the research also indicated that the number of the rings in the air holes hardly influences the modal cutoff. It is important to note that the utilization of the $V$ parameter method for identifying the single-mode operation regime for the PQF is only suitable for the PQF with a smoothly changing index fiber.

Zhao *et al.*[70] verified the invalidity of the $V$ parameter if the fiber possessed isolated high refractive regions around the core. For instance, the $V$ parameter is available for the six-fold Stampfli-type PQF but not for the eight-fold or ten-fold Penrose-type PQFs. For the fiber with isolated high refractive regions, the normalized effective mode area $A_{\mathrm{eff}}/a^2$ ($a$ is the lattice constant) can be used to effectively estimate the modal cutoff for the single-mode operation regime by observing the sudden change of the second-order $A_{\mathrm{eff}}$[102].

Similar to the $V$ parameter equation, the NA is also associated with the refractive index of the core and the cladding of the fiber. High NA fibers offer a broad spectrum of applications, including high-power lasers, fluorescence monitoring, and efficient light collection. Owing to the limited transparent solids to deploy core and cladding materials of widely differing indices, the

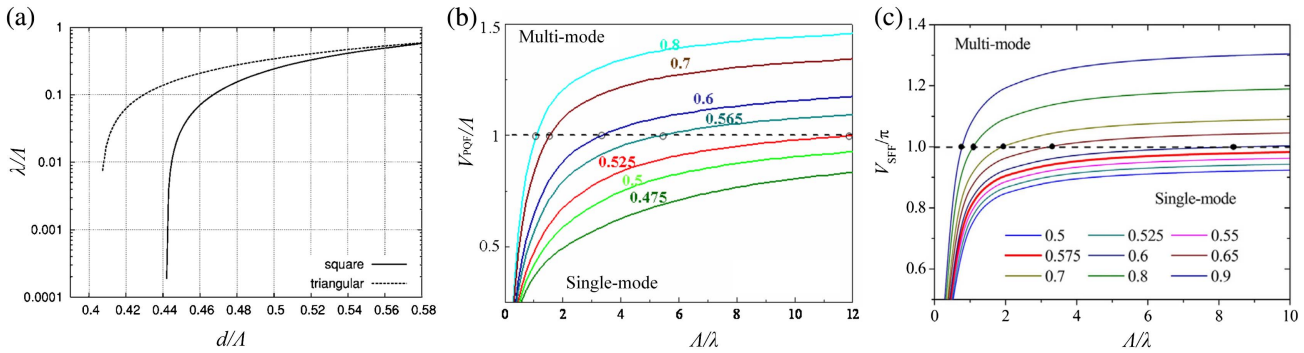


**Fig. 5.** (a) Phase diagram of the second-order mode for the eight-air-hole-ring square and the triangular PCFs[100]. (b) The normalized $V$ parameter for the Stampfli-type PQF[68]. (c) The normalized $V$ parameter for the Sunflower-type PQF[85].

conventional step-index silica core fiber could yield a maximum NA value of 0.6. By optimizing the air-filling fraction, Wadsworth *et al.*[103] proposed a 41 m PCF with a very high NA, 0.9. To further increase the NA, Paul *et al.*[104] proposed a Stampfli-type PQF with a silicon nanocrystal-filled ellipse core that could achieve an ultra-high NA of the order of 0.92 at the wavelength 1.0 μm for both the $x$-polarization and the $y$-polarization. The value of the NA was inversely proportional to the wavelength. At a longer operating wavelength of 2.6 μm, the value of the NA decreased to 0.68 in the PQF[105].

### 3.1.2. Flexibly engineered dispersion

In the communication field, dispersion is a crucial performance parameter for optical fibers. This is attributed to the fact that a too large dispersion during the signal propagation can cause serious error rates. Of course, specific systems might require higher dispersion values or larger negative dispersions. However, for the dispersion of the fundamental mode of PQFs, the total dispersion can be calculated with a sum of the material dispersion (related to the fiber material) and a waveguide dispersion (depending on the fiber structure). Therefore, PQFs with unprecedented freedom make the dispersion optimization much more flexible and offer an excellent fiber platform for their applications.

Achieving a flattened and near-zero dispersion by optimizing the size or position of the near-core air holes is one of the most well-known features of property controllability. Low and flattened dispersion benefits optical communications, wavelength-division multiplexing systems, and supercontinuum generation. The six-fold Stampfli-type PQF[68] and the three-size-hole PQF[106] achieved an ultra-flattened dispersion of 0 ± 0.05 ps/(nm km) and 6.0 ± 3.0 ps/(nm km) in a broadband of ~300 nm, respectively. A gradient eight-fold Stampfli-type PQF[107] and a Ge-doped silica six-fold PQF[99] provided a dispersion of 3.7 ± 0.89 ps/(nm km) and 12.5–29.5 ps/(nm km), respectively. Previous studies[106,107] indicate that the adjustment of the air holes that are near to the core of the PQF helps in dispersion optimization. Therefore, the construction of a double-cladding PQF has been attracting extensive research interest in fiber engineering to realize low dispersion at $-0.25 \pm 0.31$ ps/(nm km)[108] and $-2.41 \pm 0.28$ ps/(nm km)[109]. A detailed comparison of the dispersion value and bandwidth obtained by various PQFs is presented in Table 1.

Currently, high negative dispersion fibers or dispersion compensation fibers also play an important role in high-speed wavelength-division multiplexing systems for long-distance data transmission. Owing to a high wavelength-dependent refractive index of the cladding mode and a flexible array arrangement, the PQF acts as an excellent candidate for the dispersion compensation fiber. The most popular way of engineering a dispersion compensation PQF is to construct a dual core structure that contains inner and outer cores. The mode coupling between two cores leads to the mode transition process and then to the sudden change in the combined effective refractive index at the phase-matching wavelength, which further results in a narrow negative peak of dispersion. For instance, consider a dual-core Stampfli-type PQF with a negative dispersion of −2500 ps/(nm km) in a wavelength range from 1.49 μm to 1.51 μm[69], as shown in Fig. 6(a). Enlarging the mode area of the outer cores easily provides a negative dispersion of −9600 ps/(nm km)[110], as illustrated in Fig. 6(b). In fact, the intensity of the negative dispersion dip depends on the magnitude of the sudden change of the index at the phase-matching

**Table 1.** Flattened and Near-Zero Dispersion Based on the PQF Structure.

| PQF structure | Dispersion [ps/(nm km)] | Bandwidth (nm) |
|---|---|---|
| Uniformed-hole PQF[68] | 0 ± 0.05 | 190 |
| Three-layer PQF[106] | 6.0 ± 3.0 | 300 |
| Gradient-layer PQF[107] | 3.7 ± 0.89 | 250 |
| Ge-doped PQF[99] | 12.5–29.5 | 800 |
| Double-cladding PQF[108] | −2.41 ± 0.28 | 200 |
| Decagonal PQF[71] | −0.25 ± 0.31 | 400 |
| Annular-core PQF[109] | 0 ± 0.11 | 500 |
| Thue–Morse PQF[79] | < 20 | 1000 |

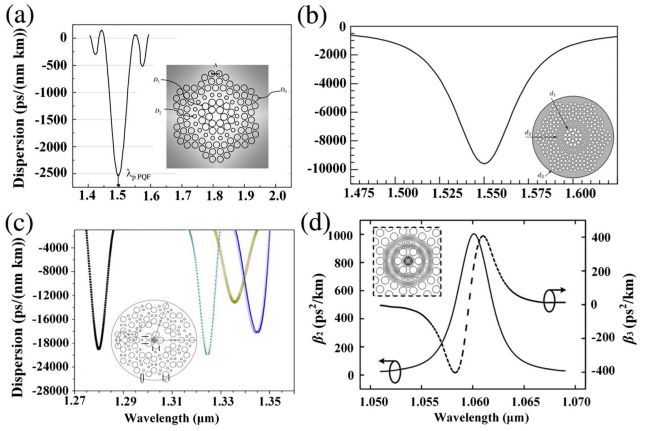


**Fig. 6.** Negative dispersion for the different PQF designs: (a) the small outer core[69], (b) the large outer core[110], and (c) the doped inner core[111]. (d) The normal dispersion for the Ge-doped PQF design[73]: the electric field distribution in the inner core and outer core at 1.06 μm and the obtained normal dispersion.

wavelength. Enlarging the air hole size of the inner core layer[77] and doping the high-index material in the inner core[111], make the coupling effect stronger. For instance, a Ge-doped inner core can cause a large negative dispersion of −22,137 ps/(nm km)[111], as shown in Fig. 6(c).

In addition, generating a high negative dispersion and achieving a high positive dispersion, together with a large mode area, is useful in chirped-pulse amplifier systems and ultrafast laser systems. This fiber serves as a stretcher for stretching the high-energy ultrashort pulses to ensure distortionless pulses. In 2010, Li *et al.*[112] reported a PQF-based 10,000 ratio stretcher in a 1 km length of fiber. They adjusted the dispersion as $\beta_2$ 35.72 ps$^2$/km by controlling the air hole size and lattice constant. In 2011, Sivabalan *et al.*[73] proposed an Yb-doped Stampfli-type PQF stretcher with a dispersion of 1000 ps$^2$/km and an inner core effective mode area of 35 μm$^2$ at 1.06 μm. This fiber could exhibit a high stretching ratio of more than 100,000. The electric field distribution and normal dispersion curves are shown in Fig. 6(d).

### 3.1.3. Strong polarization-maintaining ability

The rotational symmetry of the air-hole arrays in the PQF provides a structure that matches well with the phase of the circle-shape fundamental mode. From another aspect, an ultra-high birefringence of the guided mode can be obtained once the rotational symmetry is broken by deliberately introducing capillaries with different wall thicknesses or by designing an asymmetric porous cladding surrounding[76,87]. Moreover, compared with the conventional polarization-maintaining fiber, such as the elliptical core, the bow-tie, or the Panda fibers that generally require two constituent materials with different thermal explosion coefficients, the PQF is highly insensitive to temperature because of only one background material (silica)[76].

In 2014, a twin bow-tie polymer PQF was reported to realize a birefringence of $2.43 \times 10^{-3}$ at a wavelength 2 μm by breaking

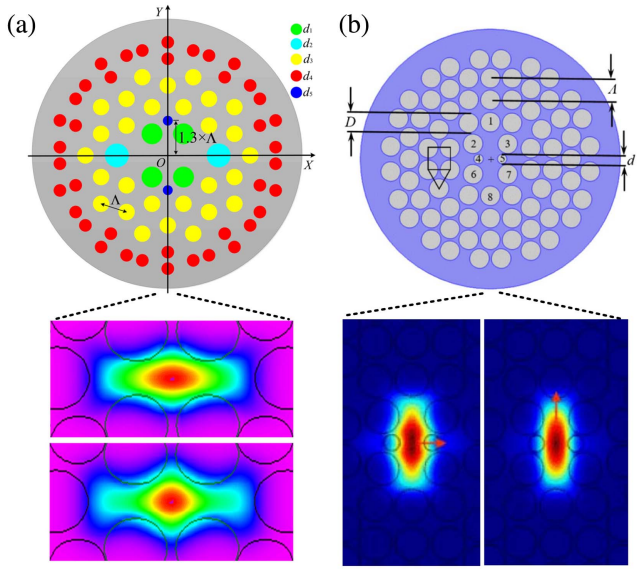


**Fig. 7.** High birefringence silica-based PQF at 1.55 μm obtained by breaking the structure symmetry. (a) The Penrose-type PQF with a birefringence of $1.4207 \times 10^{-2}$[114]. (b) The Stampfli-type PQF with a birefringence of $3.86 \times 10^{-2}$[71].

the symmetry of the *x*- and *y*- polarization electric field distribution of the guiding mode[76]. In the same year, Su *et al.* arranged four small circular air holes in the core region to squeeze the *x*-polarization electric field distribution in order to obtain a birefringence of $2.88 \times 10^{-2}$ at a wavelength of 2 μm[113]. To further exploit the near-core air hole's dependence on the birefringence, five different air holes were first used to obtain a birefringence of $1.4207 \times 10^{-2}$ at 1.55 μm[114] [Fig. 7(a)]. The simulation results indicate that at a certain wavelength, the birefringence value is influenced by the change of the air hole size, the lattice constant, and the air-filling fraction. Two mobile air holes at both sides of the core in the *x*-axis direction could be controlled to obtain an ultra-high birefringence of $3.86 \times 10^{-2}$ at 1.31 and 1.55 μm[71] [Fig. 7(b)]. In 2019, based on a $ZrF_4$-$BaF_2$-$LaF_3$-$AlF_3$-NaF PQF, Liu *et al.*[115] arranged two elliptical air holes in the core and achieved a maximum birefringence of $4.15 \times 10^{-2}$.

### 3.1.4. High mode-field area or high nonlinearities

According to the literature, the threshold value of the air-filling fraction for each type of microstructure fiber for maintaining an endlessly single mode and a large mode area fiber becomes possible by properly designing the air hole size. A high mode area fiber is significant for the generation of the amplifier and the laser as well as the delivery of a high-power pulse by reducing the nonlinearity, light damage, and thermal damage. The effective mode area $A_{\mathrm{eff}}$ is defined as[70]

$$A_{\mathrm{eff}} = \frac{\left(\iint I(x,y)\mathrm{d}x\mathrm{d}y\right)^2}{\iint I^2(x,y)\mathrm{d}x\mathrm{d}y}, \tag{4}$$

where $I(x, y)$ is the intensity of the transverse electric field distribution. According to Eq. (4), the size of $A_{\text{eff}}$ mainly depends on the $I(x, y)$, which is often optimized by controlling the fiber material and the lattice constant[71,75,80]. It is speculated that the more the electric field's distribution spreads, the larger the effective mode area is[85,86]. It is important to note that more distribution might cause a higher confinement loss and could be more sensitive to the bending state. Therefore, an anti-bending large mode area fiber is still the current research hotspot in the field of high-power laser systems.

For engineering this type of fiber, large mode area and single-mode propagation together with a low bending loss should be considered simultaneously. Introducing a large fiber core to increase the mode area is a common approach. However, some higher-order modes can also easily get trapped in the core. Increasing the size of the air holes of the microstructure fiber can shrink the bending loss, but this approach limits the mode area and may cause multimode propagation.

In 2014, an all-solid large-mode-area single-mode PQF with extremely low loss was designed by embedding a hexagonal quasicrystal array of slightly fluorine-doped silica rods in a silica background[116] [Fig. 8(a)]. It exhibited an effective mode area of 5197 μm$^2$ and a bending loss of 0.01 dB/m at a bending radius of 10 cm. With the same idea, an Yb-doped large-pitch PQF could support an $A_{\text{eff}}$ of 4660 μm$^2$ with a bending loss of $< 20$ μm$^2$[75] [Fig. 8(b)]. In fact, a large fiber core ($> 100$ μm) might give rise to the trapping of a second-order mode or higher modes. To solve this conflict, a silica-based six-fold gradient-diameter Sunflower-type PQF with five rings of air holes was proposed, as shown in Fig. 8(c)[91]. The small inner air holes constituted the near-core cladding to promote single-mode propagation and increase the mode area [Fig. 8(d)], while the large outer holes made up the outer cladding to better confine the guiding mode and reduce bending loss. Under optimal structural parameters, the fiber could realize an $A_{\text{eff}}$ of 3110 μm$^2$ and a low bending loss of $8.04 \times 10^{-6}$ dB/m at a bending radius of 15 cm at the wavelength of 1.55 μm. This engineering strategy offers an approach for balancing the large mode area, single-mode propagation, and low bending loss.

For certain fiber structures, the $A_{\text{eff}}$ value is an inversely proportional function of the nonlinear coefficient $\gamma$ at a certain wavelength. $\gamma$ is easily deduced as[71]

$$\gamma = \frac{2\pi n_2}{\lambda A_{\text{eff}}}, \tag{5}$$

where $n_2$ is the nonlinear coefficient of the core material. The fiber with a high $\gamma$ or a highly nonlinear fiber has already attracted tremendous research interest in the fields of wavelength conversion, optical parametric amplification, supercontinuum generation, high-power laser, etc. To obtain a high nonlinear coefficient, three common approaches have often been investigated for the PQF microstructure fiber.

The first approach involves the advantage of flexibly optimizing the PQF structure. Squeezing the fiber core can push the light to gather in the core to increase the nonlinearity. For instance, Su *et al.*[76] proposed a dual-concentric core structure (lattice constant ~ 1.0 μm) and a twin bow-tie structure (lattice constant ~ 3.3 μm) [Fig. 8(e)] and achieved a $\gamma$ of 33.4 W$^{-1}$km$^{-1}$ at 1.55 μm and 118 W$^{-1}$km$^{-1}$ at 2.0 μm. In 2018, Kim *et al.*[109] used an annular core Stampfli-type PQF to shrink the core layer [Fig. 8(f)] to obtain a high nonlinearity and a very low $A_{\text{eff}}$ ($< 5.6$ μm$^2$) with a lattice constant of 2.09 μm. Moreover, an ultra-wide band and nearly zero

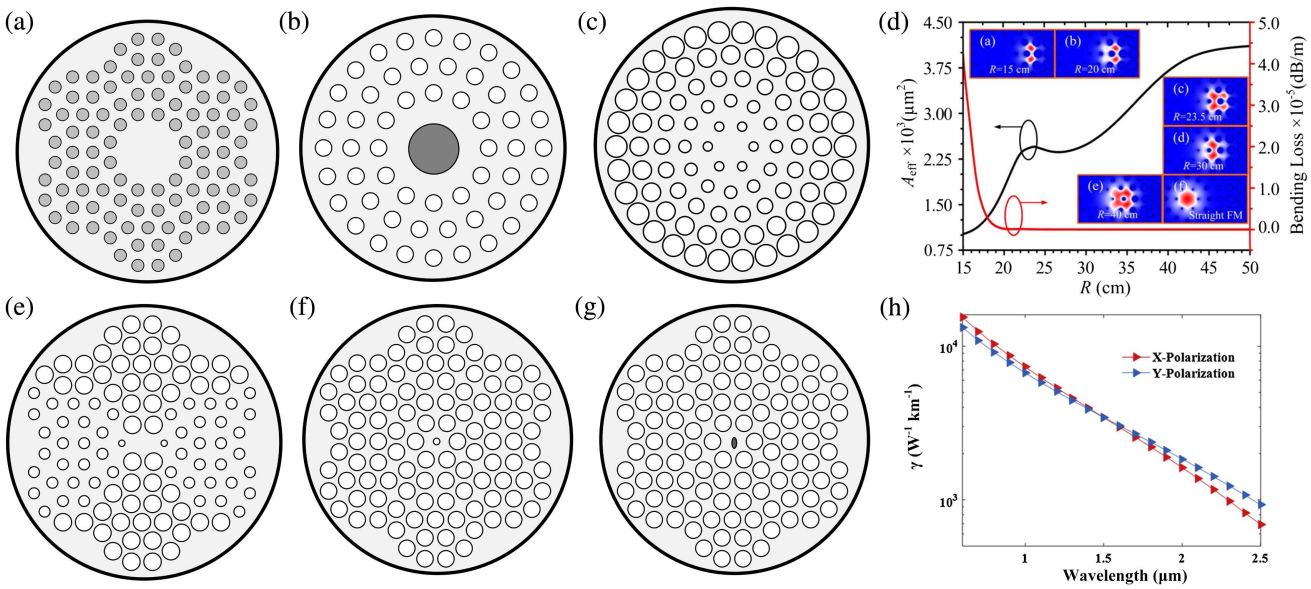


**Fig. 8.** (a)–(d) Large mode area PQF and (e)–(f) highly nonlinear PQF. (a) The large-core PQF[116]. (b) The Yb-doped large pitch PQF[75]. (c) The gradient-diameter Sunflower-type PQF [with a large effective mode area and a low bending loss shown in (d)][91]. (e) The twin bow-tie silica-based PQF[76]. (f) The annular core Stampfli-type PQF[109]. (g) The tellurite elliptical core PQF [with high nonlinearity shown in (h)][117].

ultra-flattened dispersion of 0 ± 0.11 ps/(nm km) from 1.15 μm to 1.65 μm was also obtained, which was highly expected to be applied in the supercontinuum generation.

The second approach involves the arrangement of a high-refractive-index material dielectric cylinder with a high nonlinear coefficient in the core. Benefiting from the mode distribution in the high-index region, the guiding mode can present a large $\gamma$ value. Maheswaran *et al.*[117] designed a tellurite elliptical core PQF [Fig. 8(g)] and realized a nonlinear coefficient $\gamma$ of $1.54 \times 10^4$ $W^{-1}km^{-1}$ at a wavelength of 0.6 μm. The $\gamma$ value is a hundred times that of the structure-optimized PQF, as illustrated in Fig. 8(h). Finally, if the material of the elliptical core is replaced with chalcogenide, which has a higher nonlinear refractive index, then the generated $\gamma$ reaches as high as $4.72 \times 10^4$ $W^{-1}km^{-1}$ at a wavelength of 1.0 μm[118]. In 2019, Amiri *et al.*[119] designed a $Ge_{20}Sb_{15}Se_{65}$-embedded rectangular-slotted PQF that exhibited a high $\gamma$ of $6.161 \times 10^3$ $W^{-1}km^{-1}$. Moreover, the birefringence reached a spectacular value of 0.146.

## 3.2. Applications of PQF

### 3.2.1. Specific fibers in optical communication systems

Benefiting from the optical properties of the PQFs analyzed in Section 3.1, PQFs are considered potential candidates for communication fibers and specific fibers in optical communication systems. However, for the communication PQF transmitting signal, due to the limitation of the current fabrication technique, there still exists a gap that needs be bridged for its practical applications. For the specific PQF utilized in optical systems in a laboratory, great possibilities can be achieved experimentally. For instance, a PQF with a flattened, near-zero dispersion, a low nonlinearity, and a low confinement loss can be used as wavelength-division multiplexers and interferometer sensors. The PQF's high birefringence can be used for polarization control in fiber optic sensors and high-precision optical instruments. Moreover, a high-normal-dispersion PQF can stretch high energy ultrashort pulses. Thus, it can serve as a high-quality pulse stretcher in laser systems. In particular, the hollow-core PQF with two PBGs yields new insight into propagation mechanism, which is promising for high-power soliton delivery and gas-phase nonlinear optics. Therefore, the controllable optical properties endow the unique PQF with great potential in engineering-specific fibers for communication systems.

### 3.2.2. PQF-based OAM transmission

OAM modes have attracted significant research interest due to their unique spiral phase front. Its theoretically unlimited topological charge and stable propagation of orthogonal spatial modes could be utilized in mode-division multiplexing systems to solve problems with dramatic transmission of data in current networks. Therefore, engineering a high-quality OAM fiber is the key to OAM mode propagation. The propagation performances (such as the effective index separation $\Delta n_{\text{eff}}$ between the constituent HE/EH modes in the same LP group, the OAM mode number, and the optical properties of the OAM mode) should be considered and balanced. Benefiting from a natural rotational structure that matches well with the circular phase configuration of the OAM mode, PQFs exhibit a superiority and priority for OAM transmission when compared with conventional PCFs.

In 2016, Zhang *et al.*[120] proposed a Sunflower-type OAM PQF that supported 14 OAM modes with a $10^{-3}$ level of $\Delta n_{\text{eff}}$ and < 46.38 ps/(nm km) in 1.25–2.0 μm band. The rotational symmetric cladding offers a structure that matches well with the OAM phase configuration, as indicated by the normalized intensity of all supported vector modes. Enlarging the radius of the central air hole extends the room for holding higher order OAM modes and then increases the number of OAM modes to 26[121]. However, these PQFs suffer from large dispersion, especially the high-order OAM modes. To reduce the dispersion, a dual-cladding Stampfli-type PQF was first proposed with a $\Delta n_{\text{eff}}$ of $10^{-2}$ order and a low and flattened dispersion [with a maximum variation of 19.736 ps/(nm km)][95]. The key in this method is the optimization of the dual-cladding parameters. The cross-section of the PQF, the electric field distribution, and the helix phase are plotted in Fig. 9(a). By designing a dual-core Sunflower-type PQF and achieving dual-core mode coupling [Fig. 9(b)][122], a negative dispersion of up to −3039.45 ps/(nm km) for the OAM mode $HE_{31}$ could be realized. This approach offers guidance for dispersion compensation for OAM modes. Moreover, using controllable $GeO_2$-doped silica can adjust the property of the carrying quantized OAM modes [Fig. 9(c)][123]. Utilizing ultra-large central air cores can significantly improve the capacity of the signal channels of the OAM fiber [Fig. 9(d)][124].

Based on the numerous theoretical studies mentioned above, Arsene *et al.* experimentally fabricated a ring-core fiber with hybrid cladding, consisting of air holes organized in a first circular ring surrounded by hexagonal ones [Fig. 10(a)][88]. The fiber supported 14 OAM modes and exhibited a $\Delta n_{\text{eff}}$ of $2.13 \times 10^{-3}$ at 1.55 μm. Owing to the used stack-and-draw fabrication technique, the positions of the inner circular air hole should be well controlled. The "fork-like" inference fringes from the 1.2 m OAM fiber also confirm the topological charge, as shown in Fig. 10(b).

## 3.3. PQF-based sensor

Optical fiber sensors have been widely studied and applied in the fields of life science, biochemistry, medicine, and environmental protection due to their potentially significant advantages including compact structure, *in situ* monitoring, label-free detection, and anti-electromagnetic interference[125]. Owing to the high degree of freedom, PQFs have been considered an excellent candidate for fiber platforms and for fiber sensors. To date, two types of PQF-based sensors have primarily been reported. One is based on the pure silica background PQF that can generate an external parameter-relative interference spectrum. The summit or dip of the interference fringe shifts with the variation of the targeted parameters (temperature, pressure, refractive

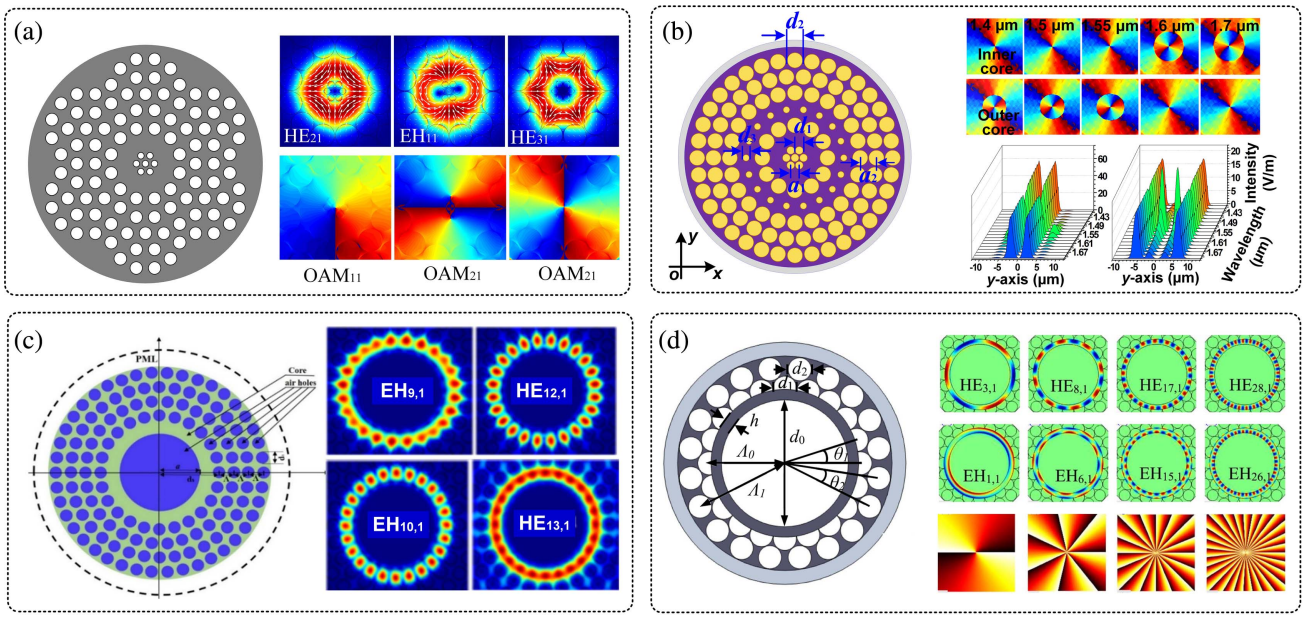


**Fig. 9.** OAM-supported PQF. (a) The dual-cladding Stampfli-type PQF, and the electric field distribution and the helix phase[95]. (b) The dual-core dispersion compensation of the Sunflower-type PQF, and the electric field distribution[122]. (c) The $GeO_2$-doped Sunflower-type PQF, and the electric field distribution[123]. (d) The $GeO_2$-doped Sunflower-type PQF, and the electric field distribution and the helix phase[124].

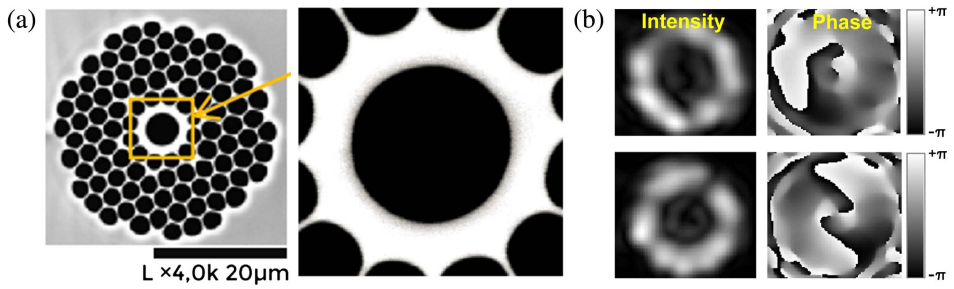


**Fig. 10.** (a) The SEM image of the fabricated ring-core PQF[88]. (b) The measured CCD images of the OAM with $l = 1$ (top) and $l = 2$ (bottom) output signals and with (left) intensities and (right) phases.

index, and humidity). For instance, for temperature and pressure sensing, Revathi *et al.*[126] proposed a dual-core PQF consisting of two cores separated with an air hole in the cross-section, as shown in Fig. 11(a) (left). The mode coupling between the two cores leads to a transmission spectrum [Fig. 11(a) (right)] that is sensitive to the photo-elastic effect and thermo-optic effect. The sensitivities for temperature and pressure are 20 pm/°C and −10.5 nm/MPa, respectively. If the core of the PQF is embedded with numerous air holes, then the frequency range for the sensor can fall into the terahertz regime[127]. It is expected to be meaningful for chemical detection of water, ethanol, benzene, etc.

Another type of PQF sensor is based on the optical phenomenon, namely, the surface plasmon resonance (SPR) that occurs from the coupling between the surface plasmon wave and the electromagenetic wave that propagates at the interface between a coated metal film and a dielectric medium[81], which is presented in Fig. 11(b). For the metal-coated fiber, the wave vector of the surface plasmon wave is associated with the refractive index of the surrounding medium, which thus renders SPR-based fibers a sensitive technique to detect the index variation of liquid concentration. In general, the SPR-based fiber sensor exhibits very high sensitivity owing to the strong coupling effect of the evanescent wave with the analyte. Microstructure fibers, such as a holes-containing-cladding PQF, offer multiple sophisticated measures for metal film deposition and targeted-liquid filling. For example, with a central hole coated with a 40-nm-gold layer of PQF[81], strong excitation of the surface plasmon polariton (SPP) occurs by the core mode, facilitating a maximum refractive index (RI) sensibility of 6000 nm/RIU and a resolution of $1.6 \times 10^{-6}$ in the RI range from 1.45 to 1.46. If a layer surrounding the fiber[128] is deposited with an indium tin oxide film [Fig. 11(c)], then the average sensitivity can be boosted to 8750 nm in the analyte RI range between 1.33 and 1.39.

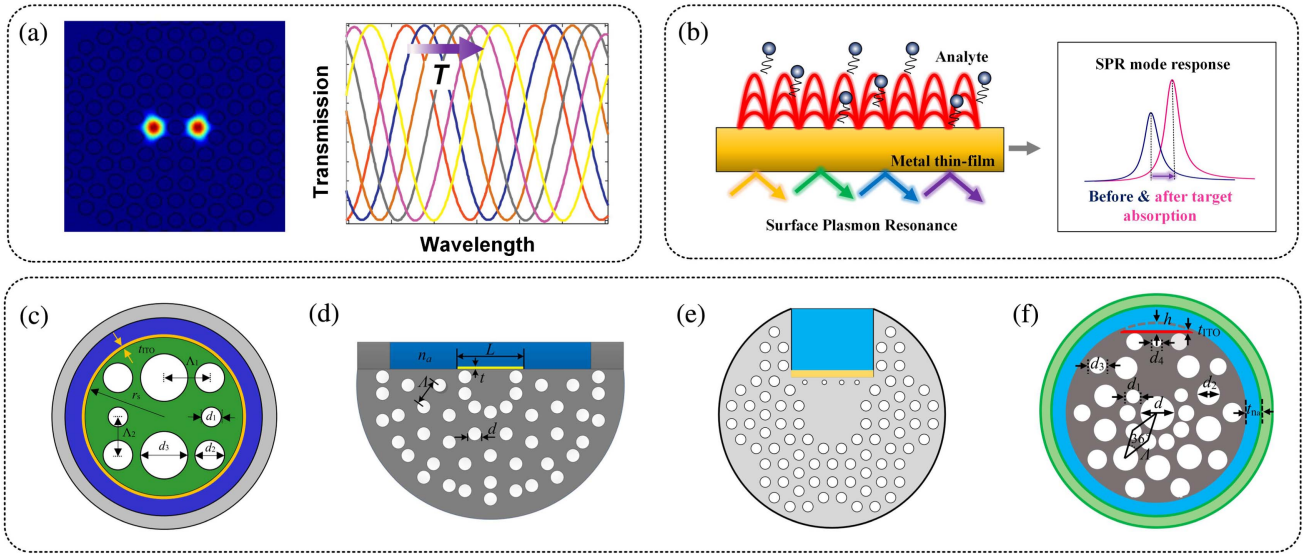


**Fig. 11.** PQF-based sensor. (a) The dual-core PQF (left), and the interference spectrum used for sensing the external temperature (right)[126].(b) The mechanism of the surface plasmon resonance PQF sensor. When the sensor is put in the target analyte, the coupling loss peak shifts. (c) The Stampfli-type PQF with a surface-coated ITO layer[128]. (d) The Penrose-type PQF with a D-shaped analyte channel[89]. (e) The U-shaped Stampfli-type PQF[90]. (f) The hybrid-size air hole PQF with a micro D-shaped analyte channel[129].

To further enhance the coupling effect and controllability, a six-fold trapezoidal analyte-channel PQF is reported with a maximum sensitivity of 17,000 nm/RIU in the RI range from 1.40 to 1.44[84]. This method demonstrates the sensitivity optimization by increasing the contacting area between the analyte and guiding mode. Based on this idea, a Penrose-type D-shaped PQF sensor [Fig. 11(d)] and a U-shaped Stampfli-type PQF sensor [Fig. 11(e)] were proposed, which offered a maximum sensitivity of 34,000 nm/RIU[89] and 33,600 nm/RIU[90], respectively. In 2021, based on the D-shaped PQF, Liu *et al.*[129] demonstrated an ultra-high sensitivity of 62,000 nm/RIU by enlarging the guiding core radius and then enhancing the coupling effect [Fig. 11(f)]. In the same year, they designed a twin D-shaped PQF with a 28-nm-thick silver film coated on the top and bottom side for methane sensing[130]. This sensor provides accurate gas sensing toward the 0%–3.5% methane concentration range.

Most of the SPPs at the metal/fiber interface reported in previous studies are excited by the common Gaussian fundamental mode[81,84,89,90,126,128–130]. Excitation by the OAM mode, however, has rarely been investigated for the SPR sensor. Recently, an SPR fiber biosensor was theoretically proposed based on a Stampfli-type PQF with one air hole coated with a gold thin film, which realized the excitation of the SPP mode by using the robust transmission of the OAM mode[131]. The profile of the designed PQF sensor is presented in Fig. 12(a). The proposed OAM-SPR fiber sensor exhibited an RI sensitivity of 4466.5 nm/RIU and a resolution of $2.3 \times 10^{-5}$ RIU in a broad RI range from 1.36 to 1.435. The basic setup for the RI detection is illustrated in Fig. 12(b). Moreover, a comparative analysis of the performance parameters of the PQF-based sensors was carried out in terms of structure, sensitivity, bandwidth, and resolution, which is presented in Table 2.

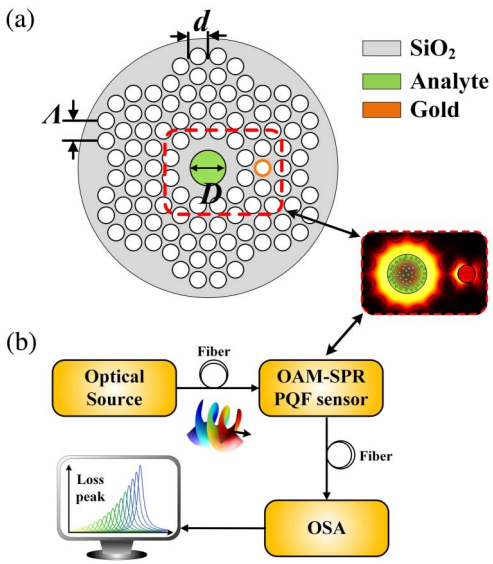


**Fig. 12.** (a) Profile of the OAM-SPR photonic quasi-crystal fiber sensor[131]. The figure outlined with the red rectangular dotted line shows the coupling field distribution. (b) Basic setup of the proposed fiber sensor for refractive index sensing.

### 3.4. PQF-based filter

In the SPR-based PQF for the sensor application mentioned above, the fiber often possesses a circular core and exhibits a very small birefringence. If the SPP modes are excited by the *x*-polarization or the *y*-polarization of the core mode in a high-birefringence fiber, then the corresponding polarization mode gets filtered because of the large coupling loss originating from the energy transformation. This type of SPR-based PQF can serve

**Table 2.** Performance Parameters of the PQF-Based Sensors.

| Structure | Sensitivity | Range | Resolution |
|---|---|---|---|
| Dual-core all-silica PQF[126] | 20 pm/°C | 0°C–1000°C | / |
| Porous-core PQF[127] | 18.03 THz/RIU | 0.5–1.5 THz | $7.75 \times 10^{-5}$ |
| Hole-coated gold layer PQF[81] | 6000 nm/RIU | 1.45–1.46 RIU | $1.0 \times 10^{-6}$ |
| ITO-surrounded PQF[128] | 35,000 nm/RIU | 1.26–1.38 RIU | $2.86 \times 10^{-6}$ |
| Trapezoidal-channel PQF[84] | 17,000 nm/RIU | 1.40–1.44 RIU | $1.64 \times 10^{-5}$ |
| D-shaped PQF[89] | 34,000 nm/RIU | 1.415–1.427 RIU | / |
| U-shaped PQF[90] | 33,600 nm/RIU | 1.420–1.436 RIU | / |
| Large-core D-shaped PQF[129] | 62,000 nm/RIU | 1.40–1.44 RIU | $1.0 \times 10^{-6}$ |
| Twin D-shaped PQF[130] | 6.643 nm/% (methane) | 0%–3.5% (concentration) | / |
| Ring-core PQF[131] | 4466.5 nm/RIU | 1.36–1.435 RIU | $2.3 \times 10^{-5}$ |

as a polarization filter. In 2018, an SPR-based birefringence Sunflower-type PQF was proposed for polarization filtering in the visible wavelength regime[87]. By arranging two large air holes and filling RI-matching liquids in a small air hole coated with a gold film layer, the fiber enabled the filter to work at a wavelength of 0.55–0.68 μm by adjusting the thickness of the film. The resonance loss of the *y*-polarization reached 11,707 dB $m^{-1}$ and the extinction ratio exceeded 100 dB.

### 3.5. PQF-based supercontinuum generation

Supercontinuum generation (SC) is one of the most significant applications of the PQF due to its high nonlinear coefficient by the shrunken core. The spanning spectrum of SC sources has been extended from the visible to near-infrared wavelengths, which enables various applications in optics, medicine, and biology. According to the nonlinear Schrödinger equation, it can be deduced that the SC performance mainly depends on the fiber parameters (dispersion, nonlinear coefficient, confinement loss, length, etc.) and pump pulse parameters (pulse power, duration, polarization state, etc.). The microstructure fiber with controllable optical properties is being considered to be the dominant medium in the SC generation. Considering its simple fabrication, Sunflower-type PQFs are often employed for engineering this type of fiber.

In 2015, Medjouri *et al.*[132] reported a Sunflower-type PQF with a defective core and a small ring of air holes for the SC generation [Fig. 13(a)]. However, the achieved $\gamma$ is less than 16 $W^{-1}$ $km^{-1}$ at 1.2–1.8 μm, and the generated narrow band is less than 600 nm because of the adopted pure silica background (nonlinear RI $n_2 = 3.0 \times 10^{-20}$ $m^2/W$) of the PQF. With the same background material, Krishna *et al.*[133] also obtained a low $\gamma$ value and a bandwidth of ~600 nm of SC based on uniformed-hole Sunflower-type PQFs. To increase the $\gamma$ and broaden the bandwidth of SC, the materials with a high nonlinear RI, such as tellurite, chalcogenide, and fluoride glass, have been used as the common background. In 2016, Ahmad *et al.*[134] proposed two $As_2S_3$ and $As_2Se_3$ Sunflower-type PQFs. By customizing the zero dispersion wavelength in the 2.0–2.5 μm range, they achieved a wide band of SC in the wavelength range from 1.2 μm to 9.3 μm with a duration of 50 fs and 1 kW power pulse focusing into a 0.5 cm long $As_2Se_3$ PQF. In 2017, based on a $As_2Se_3$ Stampfli-type PQF with a high $\gamma$ of 2079 $W^{-1}km^{-1}$, Zhao *et al.*[83] demonstrated an SC generation at 1.0–10.2 μm and 1.0–12.5 μm for *x*- and *y*-polarized modes, respectively [Fig. 13(b)]. In general, the spectral broadening in the PQF is first dominated by the self-phase modulation effect, followed by soliton fission from the high-order solitons to the fundamental solitons. The solitons then experience a continuous red or blue shift due to the Raman effect (Raman self-frequency shift). If the fiber parameters are selected properly, then a mid-infrared broadband ultraflat-top supercontinuum (with $> 4$ dB) can be generated via the optical wave breaking mechanism, which is reported in the all-normal dispersion (ANDi) $Ge_{15}Sb_{15}Se_{70}$ chalcogenide Sunflower-type PQF [Fig. 13(c)][135]. With the same idea, the chalcogenide $Ge_{11.5}As_{24}Se_{64.5}$ PQF can realize an ultra-wide SC with a band from 2 μm to 15 μm for both *x*- and *y*- polarized modes [Fig. 13(d)][82].

## 4. Challenges and Prospects

In this section, the challenges and prospects of the physical study and application of PQFs are outlined. Light-guiding mechanisms of PQFs primarily need further clarification because light transmission in the transverse $x$–$y$ plane is not a Bloch wave travel due to the lack of a Bravais lattice, even though the total reflection mechanism can explain it. Then, herein, the possible preparation methods of quasiperiodic air-hole arrays in PQFs are also discussed since it is hard to assemble the aperiodic

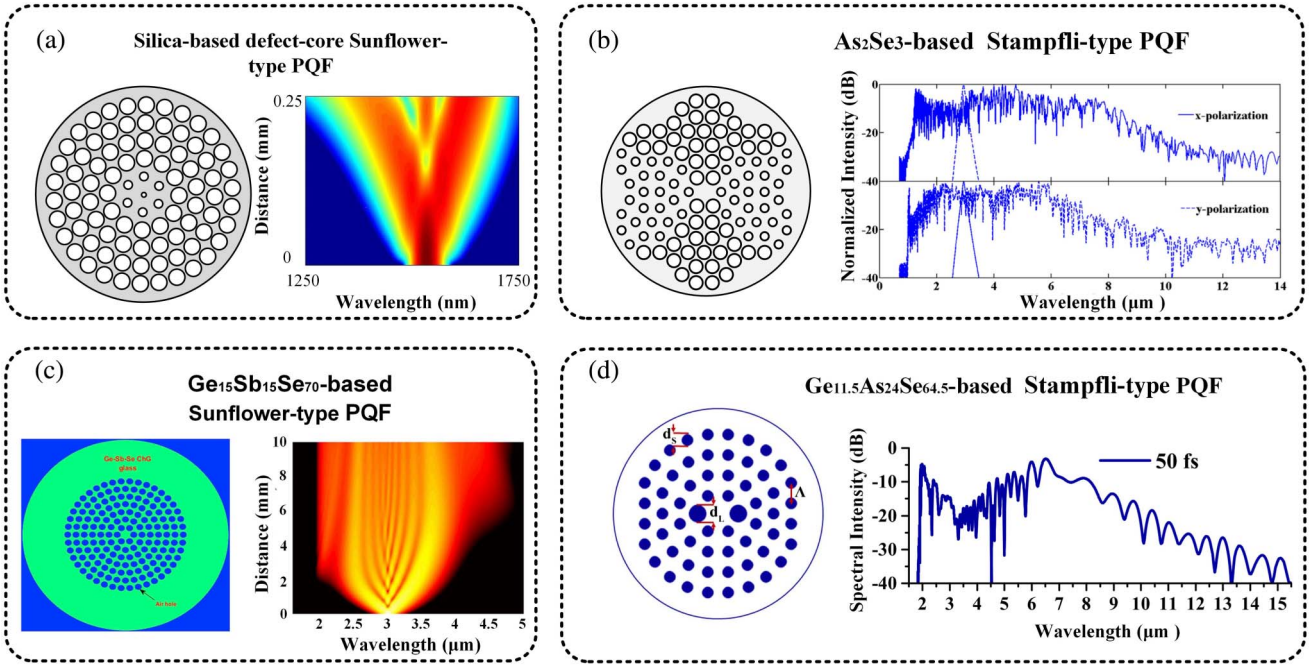


**Fig. 13.** Supercontinuum generation based on the highly nonlinear PQF. (a) The silica-based Sunflower-type PQFs with a defect-core[132]. (b) The $As_2Se_3$-based Stampfli-type PQF[83]. (c) The $Ge_{15}Sb_{15}Se_{70}$-based Sunflower-type PQF[135]. (d) The $Ge_{11.5}As_{24}Se_{64.5}$-based Stampfli-type PQF[82].

capillaries and rods using the stack approach, as stacking arrays are naturally periodic. Finally, the potential applications of PQFs, with their unprecedented degrees of freedom and unique cladding structures, are discussed.

## 4.1. Challenges

### 4.1.1. Guiding mechanisms in solid-, hollow-, and hybrid-core PQF

Owing to the aperiodic lattice arrays of the air holes running along the PQF, the guiding mechanism of the fundamental mode is not exactly similar to the PCF. Light-guiding mechanisms of PQFs primarily need further clarification because 1) the light transmission in the transverse $x$–$y$ plane is not similar to the Bloch wave travel due to the lack of a Bravais lattice, even though the total reflection mechanism can explain it. 2) Local (not completed) PQ arrays are introduced in the PQF so that the photonic band structure of the PQ previously demonstrated cannot exactly describe locally introduced-array PQFs. Although various and plentiful studies have been performed on PQFs, most of these studies focused on the mode analysis based on some commercial softwares. Comprehensive understanding of the PQF's guiding mode is still not sufficient. Moreover, for hybrid-core PQFs (composed of air holes and high-index-doped silica rods arranged around a silica core), how the combined effect of total internal reflection and PBG dominates the guiding feature needs to be identified because PBGs and rich localization states of PQFs that differ from PCFs may cause different anti-resonant reflection, leading to changes in the combined effects.

### 4.1.2. Fabrication method of PQF

Although PQFs with various outstanding propagation performances and important potential applications have been demonstrated, the primary and the biggest current challenge is the fiber fabrication for specifically quasiperiodic-arranged air-hole arrays. According to the current fiber-drawing technique and the prevailing stack-and-draw approach, it is hard to assemble the aperiodic capillaries and rods via the stacking approach because stacking arrays are naturally periodic. With appropriate arrangement and operation, only a limited number of capillaries (such as the ring of air holes near the core) can be drawn following quasi-periodicity[88]. The drilling technique supports the adjustment of the array pattern[136], the hole size, and the lattice constant, but it is limited to fabricating only a circular shape and a restricted number of air holes. The extrusion method allows a wide range of design freedom[137]. However, the material of the PQF is limited to soft glass. Considering the cost, preparation precision, design freedom, and ease of fabrication, the sol-gel casting technique might be suitable for the fabrication of a PQF featuring aperiodic hole arrays with circular, elliptical, or rectangular holes[138]. In 2005, Ryan *et al.*[139,140] demonstrated this sol-gel casting technique for deriving microstructure fibers and found it suitable for PQF fabrication because of its affordable wide-range design flexibility for each hole position. Cross-sectional images of sol-gel-derived microstructure fibers are shown in Figs. 14(a)–14(d).

In addition to the sol-gel casting technique, the development of 3D printing techniques can offer a direct one-step high-resolution solution on the end face of a standard single-mode fiber. In 2020, optical waveguide segments with PCF designs were

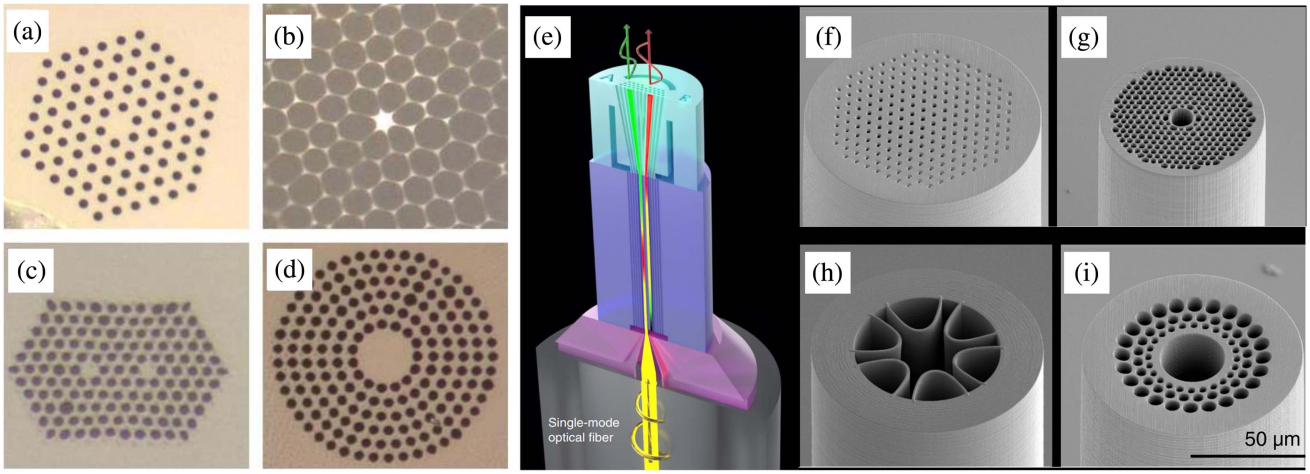


**Fig. 14.** (a)–(d) Cross-sectional images of the sol–gel-derived microstructure fibers[139] and the 3D printing of PCF[141]. (a) The endlessly single-mode design. (b) The high delta, highly nonlinear fiber. (c) The dual-core structure. (d) The circular-core PCF. (e) The PCF polarization beam splitter enabled by the 3D printing of the PCF designs. A beam with an arbitrary polarization (yellow beam) is split into its horizontal (red beam) and vertical (green beam) polarization components. (f) The helically twisted coreless PCF. (g) The PBG hollow-core PCF. (h) The anti-resonant hollow-core PCF. (i) The fractal ring-core PCF.

successfully fabricated by 3D printing[141]. The design and fabrication of an all-fiber integrated PCF polarization beam splitter are illustrated in Fig. 14(e). SEM images of different classes of 3D-printed PCF designs are shown in Figs. 14(f)–14(i).

Herein, for PQF fabrication, a brief description of the sol-gel casting technique is provided. This technique mainly involves five procedures, as shown in Fig. 15. (1) Assembling the mold, which includes the arrays of mandrel elements following a certain pattern, is, when compared to other methods, a significant advantage because of the independently controllable hole size, spacing, and position. In this way, any complex PQF can be fabricated with the achievement of the mold. (2) Filling the mold with colloid silica with an average particle size of 40 nm. Therefore, the minimum size of the air hole in the designed PQF should be around the order of around $10^{-2}$ nm. (3) Reducing the pH level to facilitate the sol-gel process. (4) Removing the mandrel elements from the gel body at the wet gel state. Herein, it is noted that the removal process should be carefully fulfilled owing to the fragile gel body. (5) Thermodynamically eliminating organic residue, water molecules, and transition metal contaminants from the gel body. In general, the achieved air-filling fraction at this state is small. To obtain a large air-filling fraction fiber (for nonlinear PQF), hydrofluoric acid etching or pressurizing the holes during the drawing process can help acquire more than an 87% air-filling fraction[139].

### 4.2. Prospects

Systematic explorations of PCF theory and application prospects have lasted for more than thirty years in ever-widening areas of science and technology due to their diverse structures and features. The techniques of some PCF-based optical devices, such as PCF lasers, PCF sensors, and supercontinuum sources, have

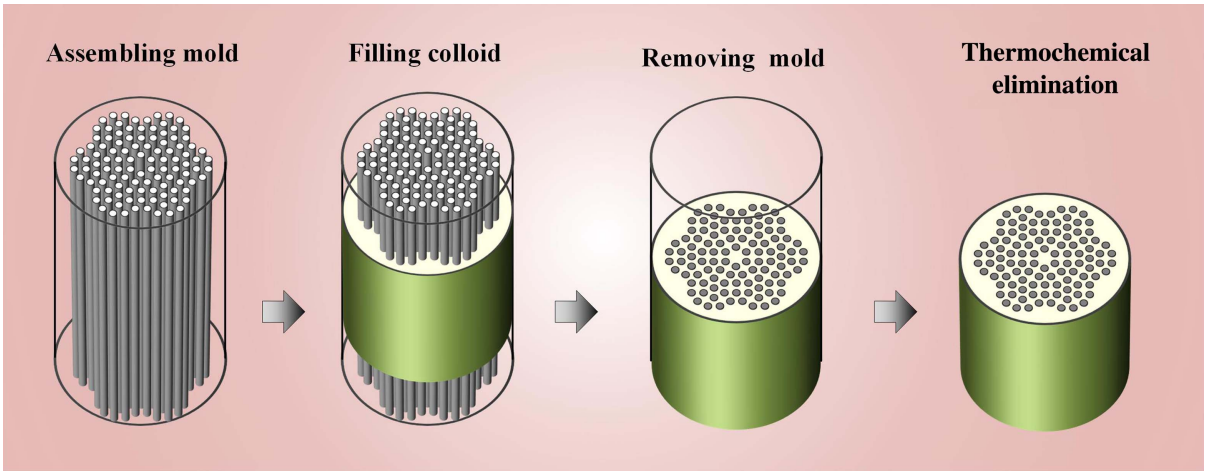


**Fig. 15.** Description of a potential preparation process of a PQF using the sol–gel method.

matured and have been commercially applied to wide linear and nonlinear optical systems. However, as a new type of microstructure fiber with diverse novel or improved properties beyond the step-index fiber, studies of PQFs are still in the preliminary stage in terms of internal mechanism and related devices. According to the characteristics of the guiding modes of PQFs and the current advances in fiber techniques, the future prospects are briefly presented in this section.

#### 4.2.1. Vortex-multiplexed communications and vortex nonlinear process

As discussed in Section 3.2.2, PQFs with rational hole arrays can be used to naturally construct a ring core for guiding the vortex mode or the OAM mode only by adjusting the hole size and the hole pitch without a high RI material-doping process for the ring core. Moreover, high degrees of structural freedom contribute to the flexible tailing of the mode propagation. Rapidly developing vortex-multiplexed systems are considered one of the next-generation, high-dimensional fiber communication technological features for addressing the soaring demand of managing data[142]. Based on the PQF structure, how to further increase the number of OAM modes (or signal-carrying channels) and enhance the transmission robustness by lifting the $\Delta n_{\mathrm{eff}}$, will be explored primarily at the communication wavelength of 1.55 μm. Previous research shows that the high-order OAM modes suffer from a very large dispersion[120–124], so the design of a near-zero dispersion PQF for all-order modes or the technique of wiping out the accumulated dispersion, still needs to be engineered. Moreover, anti-bending PQFs with a large mode area might offer a new way to reduce thermal damage and balance the single-mode operation and bending loss. With the development of PQFs, there is an increasing demand for involved intra-fiber devices, such as low-loss splices, multiport couplers, high-quality cleaves, and transformers.

To date, extensive research efforts have been devoted to the study of the OAM fiber communication systems. However, the nonlinear effects of the OAM-supported PQF have rarely been explored. It is easy to observe the nonlinear effects because of the easily obtained nonlinear length, effective fiber length, and dispersion length that are associated with various nonlinear effects, such as soliton self-frequency shift cancellation, four-wave mixing, SC generation, Brillouin scattering, parametric amplification, and parametric oscillation. Furthermore, as a multi-mode fiber, the OAM-supported PQF may introduce more novel, complex, or interesting nonlinear phenomena. Comprehensive understanding of the nonlinear behaviors of the pump pulse in an OAM-supported multi-mode fiber is crucial for the development of high-dimensional optical communication techniques and high-power pulse lasers.

#### 4.2.2. PQF-based laser

In recent years, PCFs have proved to be one of the most prevailing gain media for realizing high-power, high-quality output lasers with the natural advantages of large mode area, high heat-resistance, and polarization controllability. Similarly, as discussed in previous studies[68–87], PQFs possess higher property tunability and structure customization for maintaining large mode area, single-mode propagation, and low bending loss, which is expected to effectively break the limit of output power by restraining nonlinearity. Therefore, PQF-based gain medium for lasers is worthy of detailed investigation in terms of single-cladding fiber lasers, double-cladding large-mode-area fiber lasers, high-polarization fiber lasers, and all-solid PBG fiber lasers with fiber core (sometimes cladding) doping laser-active rare-earth elements ($Yb^{3+}$, $Nd^{3+}$, $Er^{3+}$, and so forth).

#### 4.2.3. PQF-based topologically protected mode transmission

In the past decade, the realization of photonic Floquet topological insulators has opened up an entirely new field of photonic topological insulators free of external fields and with scattering-free edge transport of visible light[143–145]. The propagation robustness, despite defects and disorder, offers the possibility of loss-free state transmission. These papers involving helical waveguides, arranged in a triangular honeycomb lattice, predict that helical PCFs are likely to exhibit robust topologically protected states. In 2016, Bandres *et al.*[146] demonstrated scattering-free unidirectional edge states in Floquet Penrose-type PQ systems that could exhibit an entirely new topological system with rich fractal (self-similar) structures of topological "minigaps." In 2019, a topological propagation system was reported based on a 2D Stampfli-triangle photonic crystal by only changing the diameters of the cylinders rather than expanding or shrinking the hole space[49]. All mentioned topological systems show great potential for achieving topological PQFs that can explore new optical phenomenon due to the topological PBG[36,49,147,148]. In fact, in 2021, a topological square PCF was theoretically proposed based on second-order corner modes by arranging the fiber configuration of $k_z > 0$[149]. However, first the issue of how to generate the topological edge state in an angular-periodic PQ with $k_z = 0$ needs to be addressed. Furthermore, the quality of the topological modes of the fiber and the corresponding applications in the linear or nonlinear systems are expected to be identified in the future.

In Floquet topological insulators, each dielectric cylinder spiral surrounds the individual center of rotation. However, if all dielectric cylinders are twisted by one rotation center[150], then the constructed solid-core PCF can generate or propagate a number of OAM modes[151]. Under an appropriate structure, the triggered coupling between the core mode and cladding mode enables the occurrence of multiple narrow dips in the transmission spectrum, which has been demonstrated with wide applications in band-rejection filters[152] and various parametric sensors[153]. Owing to structural rotation symmetry, twisted PQFs may exhibit high-quality transmission of OAM modes and may generate rich and new coupling phenomena with a number of "hot points" originating from high self-similarity.

#### 4.2.4. PQF-based grating, quantum dots-coated PQF, PQF metalens

Engineering a PQF by combining other techniques may provide opportunities for finding new photophysics and optical applications. For instance, etching a PQF with grating structures, such as fiber Bragg grating, tilted fiber Bragg grating, or long-period grating, aids in constructing parameter fiber sensors or interferometer-type fiber sensors. Coating the thin films of the quantum dots in all the air holes of the PQF can be utilized to control the field distribution and the optical properties using the electrostatic self-assembling technique[154]. In addition to the deposition of quantum dots, an ultra-thin optical metalens directly patterned on the core region of the PQF can enable light focusing, which promotes novel applications in the fields of fiber-based focusing, sensor, or imaging[155]. In summary, with unprecedented degrees of freedom and striking optical properties, PQFs are expected to be a good candidate platform for injecting liquid, gases, and quantum dots into the hollow core of cladding holes to tune guiding properties; coating or filling metal materials to enhance the SPR for sensing; or writing a long-period grating in the fiber core to facilitate the coupling between core modes and cladding modes at certain wavelengths for curvature, bending, temperature, and strain sensors. The wavelength range will hopefully be extended from the visible range to the infrared range and even to the terahertz region.

## 5. Conclusions

This review provides an in-depth and comprehensive summary of the basic concepts and current developments of PQFs in terms of their invention history, structure categories, guiding mechanisms, optical properties, potential applications, challenges encountered, and application prospects. Notably, the unique cladding arrays with rotation symmetry and long-order orientation endow the PQF with parallel-PCF propagation characteristics (including single-mode operation, high numeric aperture, flattened dispersion, large nonlinearity, etc.) with flexible optimization. The holes-containing cladding also allows for the integration of novel and functional materials inside solid-core and hollow-core PQFs. Therefore, these fibers can create new opportunities for a host of diverse areas in fiber sensors, OAM transmitting fibers, and topological fibers as well as in the fields of optical communications, biophotonics, biomedicine, ultrafast science, and quantum optics. The next decades may see the emergence of real PQF structures and more commercial PQF-based fiber devices.

## Acknowledgement

This work was supported by the Changsha Municipal Natural Science Foundation (No. kq2202295), the Scientific Research Foundation of Hunan Provincial Education Department (Nos. 22B0273 and 21A0013), the National Natural Science Foundation of China (Nos. 61405058 and 62075059), and the Natural Science Foundation of Hunan Province (Nos. 2017JJ2048 and 2020JJ4161).

## References

1. D. Shechtman, I. Blech, D. Gratias, and J. W. Cahn, "Metallic phase with long-range orientational order and no translational symmetry," Phys. Rev. Lett. **53**, 1951 (1984).
2. D. Levine and P. J. Steinhardt, "Quasicrystals: a new class of ordered structures," Phys. Rev. Lett. **53**, 2477 (1984).
3. M. Duneau and A. Katz, "Quasiperiodic patterns," Phys. Rev. Lett. **54**, 2688 (1985).
4. A. L. Mackay, "Quasi-crystals and amorphous materials," J. Non-Cryst. Solids **97–98**, 55 (1987).
5. A. N. Poddubny and E. L. Ivchenko, "Photonic quasicrystalline and aperiodic structures," Physica E Low Dimens. Syst. Nanostruct. **42**, 1871 (2010).
6. P. Stampfli, "A dodecagonal quasi-periodic lattice in two dimensions," Helv. Phys. Act. **59**, 1260 (1986).
7. H. Chen, D. X. Li, and K. H. Kuo, "New type of two-dimensional quasicrystal with twelvefold rotational symmetry," Phys. Rev. Lett. **60**, 1645 (1988).
8. D. Levine and P. J. Steinhardt, "Quasicrystals. I. Definition and structure," Phys. Rev. B **34**, 596 (1986).
9. M. Kohmoto, B. Sutherland, and K. Iguchi, "Localization of optics: quasiperiodic media," Phys. Rev. Lett. **58**, 2436 (1987).
10. L. Guidoni, C. Triché, P. Verkerk, and G. Grynberg, "Quasiperiodic optical lattices," Phys. Rev. Lett. **79**, 3363 (1997).
11. L. Voigt, M. Kubus, and K. S. Pedersen, "Chemical engineering of quasicrystal approximants in lanthanide-based coordination solids," Nat. Commun. **11**, 1 (2020).
12. A. Szabó and U. Schneider, "Mixed spectra and partially extended states in a two-dimensional quasiperiodic model," Phys. Rev. B **101**, 014205 (2020).
13. M. Sbroscia, K. Viebahn, E. Carter, J.-C. Yu, A. Gaunt, and U. Schneider, "Observing localization in a 2D quasicrystalline optical lattice," Phys. Rev. Lett. **125**, 200604 (2020).
14. U. Agrawal, S. Gopalakrishnan, and R. Vasseur, "Universality and quantum criticality in quasiperiodic spin chains," Nat. Commun. **11**, 2225 (2020).
15. E. Cherkaev, F. G. Vasquez, C. Mauck, M. Prisbrey, and B. Raeymaekers, "Wave-driven assembly of quasiperiodic patterns of particles," Phys. Rev. Lett. **126**, 145501 (2021).
16. Y. S. Chan, C. T. Chan, and Z. Y. Liu, "Photonic band gaps in two dimensional photonic quasicrystals," Phys. Rev. Lett. **80**, 956 (1998).
17. M. W. C. Dharma-Wardana, A. H. MacDonald, D. J. Lockwood, J.-M. Baribeau, and D. C. Houghton, "Raman scattering in Fibonacci superlattices," Phys. Rev. Lett. **58**, 1761 (1987).
18. Y.-Y. Zhu and N.-B. Ming, "Second-harmonic generation in a Fibonacci optical superlattice and the dispersive effect of the refractive index," Phys. Rev. B **42**, 3676 (1990).
19. C. Yue, W. Tan, and J. Liu, "Photonic band gap properties of one-dimensional Thue–Morse all-dielectric photonic quasicrystal," Superlattices Microstruct. **117**, 252 (2018).
20. W. Tan, E. Liu, B. Yan, J. Xie, R. Ge, D. Tang, J. Liu, and S. Wen, "Subwavelength focusing of a cylindrically symmetric plano-concave lens based on a one-dimensional Thue–Morse photonic quasicrystal," Appl. Phys. Express **11**, 092002 (2018).
21. B. Freedman, G. Bartal, M. Segev, R. Lifshitz, D. N. Christodoulides, and J. W. Fleischer, "Wave and defect dynamics in nonlinear photonic quasicrystals," Nature **440**, 1166 (2006).
22. C. Zhang, Z. Jiang, W. Tan, R. Ge, and J. Liu, "Non-near-field sub-diffraction focusing in the visible wavelength range by a Fibonacci subwavelength circular grating," J. Opt. Soc. Am. A **35**, 1701 (2018).
23. M. E. Zoorob, M. D. B. Charlton, G. J. Parker, J. J. Baumberg, and M. C. Netti, "Complete photonic bandgaps in 12-fold symmetric quasicrystals," Nature **404**, 740 (2000).
24. C. Jin, B. Cheng, B. Man, Z. Li, D. Zhang, S. Ban, and B. Sun, "Band gap and wave guiding effect in a quasiperiodic photonic crystal," Appl. Phys. Lett. **75**, 1848 (1999).

25. C. Jin, B. Cheng, B. Man, Z. Li, and D. Zhang, "Two-dimensional dodecagonal and decagonal quasiperiodic photonic crystals in the microwave region," Phys. Rev. B **61**, 10762 (2000).
26. M. Notomi, H. Suzuki, T. Tamamura, and K. Edagawa, "Lasing action due to the two-dimensional quasiperiodicity of photonic quasicrystals with a penrose lattice," Phys. Rev. Lett. **92**, 123906 (2004).
27. Z. Feng, X. Zhang, Y. Wang, Z. Y. Li, B. Cheng, and D. Z. Zhang, "Negative refraction and imaging using 12-fold-symmetry quasicrystals," Phys. Rev. Lett. **94**, 247402 (2005).
28. W. Zhang, W. Tan, Q. Yang, T. Zhou, and J. Liu, "Subwavelength focusing in visible light band by a Fibonacci photonic quasi-crystal plano-concave lens," J. Opt. Soc. Am. B **35**, 2364 (2018).
29. X. Zhang, Z. Li, B. Cheng, and D. Z. Zhang, "Non-near-field focus and imaging of an unpolarized electromagnetic wave through high-symmetry quasicrystals," Opt. Express **15**, 1292 (2007).
30. L. Levi, M. Rechtsman, B. Freedman, T. Schwartz, O. Manela, and M. Segev, "Disorder-enhanced transport in photonic quasicrystals," Science **332**, 1541 (2011).
31. C. Bauer, G. Kobiela, and H. Giessen, "Optical properties of two-dimensional quasicrystalline plasmonic arrays," Phys. Rev. B **84**, 193104 (2011).
32. J. Liu, Z. Fan, H. Xiao, W. Zhang, C. Guan, and L. Yuan, "Photonic bandgaps of different unit cells in the basic structural unit of germanium-based two-dimensional decagonal photonic quasi-crystals," Appl. Opt. **50**, 4868 (2011).
33. J. Liu, Z. Fan, M. Kuang, G. He, C. Guan, and L. Yuan, "Relative permittivity dependence of photonic band gaps for unit cells of the basic structural unit of two-dimensional decagonal photonic quasicrystals," Opt. Commun. **288**, 52 (2013).
34. J. Liu, Z. Fan, H. Hu, M. Yang, C. Guan, L. Yuan, H. Guo, and X. Zhang, "Wavelength dependence of focusing properties of two-dimensional photonic quasicrystal flat lens," Opt. Lett. **37**, 1730 (2012).
35. Z. Fan, J. Liu, S. Chen, H. Chang, C. Guan, and L. Yuan, "Comparative study of photonic band gaps of germanium-based two-dimensional triangular-lattice and square-lattice and decagonal quasi-periodic photonic crystals," Microelectron. Eng. **96**, 11 (2012).
36. M. Verbin, O. Zilberberg, Y. E. Kraus, Y. Lahini, and Y. Silberberg, "Observation of topological phase transitions in photonic quasicrystals," Phys. Rev. Lett. **110**, 076403 (2013).
37. Z. V. Vardeny, A. Nahata, and A. Agrawal, "Optics of photonic quasicrystals," Nat. Photonics **7**, 177 (2013).
38. J. J. Liu, H. L. Hu, W. Zhang, and Z. G. Fan, "Scatterer radius dependence of focusing properties in two-dimensional photonic quasicrystal flat lens," Photonics Nanostructures-Fundam. Appl. **12**, 138 (2014).
39. J. J. Liu, E. X. Liu, T. H. Zhang, and Z. G. Fan, "Thickness dependence of two-dimensional photonic quasicrystal lens imaging characteristics," Solid State Commun. **201**, 68 (2015).
40. J. Liu, E. Liu, Z. Fan, and X. Zhang, "Dielectric refractive index dependence of the focusing properties of a dielectric-cylinder-type decagonal photonic quasicrystal flat lens and its photon localization," Appl. Phys. Express **8**, 112003 (2015).
41. J. Liu, E. Liu, and Z. Fan, "Width dependence of two-dimensional photonic quasicrystal flat lens imaging characteristics," J. Mod. Opt. **63**, 692 (2016).
42. J. Liu, W. Tan, E. Liu, H. Hu, Z. Fan, T. Zhang, and X. Zhang, "Planar scanning method for detecting refraction characteristics of two-dimensional photonic quasi-crystal wedge-shaped prisms," J. Opt. Soc. Am. A **33**, 978 (2016).
43. B. Feng, E. Liu, Z. Wang, W. Cai, H. Liu, S. Wang, T. Liang, W. Xiao, and J. Liu, "Generation of terahertz hollow beams by a photonic quasi-crystal flat lens," Appl. Phys. Express **9**, 062003 (2016).
44. Y.-F. Zhao, Z.-M. Wang, Z.-J. Jiang, C.-X. Yue, X. Chen, J.-Z. Wang, and J.-J. Liu, "Add-drop filter with compound structures of photonic crystal and photonic quasicrystal," J. Infrared Millim. Waves **36**, 342 (2017).
45. J. Liu and Z. Fan, "Size limits for focusing of two-dimensional photonic quasicrystal lenses," IEEE Photon. Technol. Lett. **30**, 1001 (2018).
46. R. Ge, J. Xie, B. Yan, E. Liu, W. Tan, and J. Liu, "Refractive index sensor with high sensitivity based on circular photonic crystal," J. Opt. Soc. Am. A **35**, 992 (2018).
47. J. Ren, X. H. Sun, and S. Wang, "A low threshold nanocavity in a two-dimensional 12-fold photonic quasicrystal," Opt. Laser Technol. **101**, 42 (2018).
48. K. Viebahn, M. Sbroscia, E. Carter, J.-C. Yu, and U. Schneider, "Matter-wave diffraction from a quasicrystalline optical lattice," Phys. Rev. Lett. **122**, 110404 (2019).
49. B. Yan, J. Xie, E. Liu, Y. Peng, R. Ge, J. Liu, and S. Wen, "Topological edge state in the two-dimensional Stampfli-triangle photonic crystals," Phys. Rev. Appl. **12**, 044004 (2019).
50. A. Shi, R. Ge, and J. Liu, "Refractive index sensor based on photonic quasicrystal with concentric ring microcavity," Superlattices Microstruct. **133**, 106198 (2019).
51. Y. Tang, J. Deng, K. F. Li, M. Jin, J. Ng, and G. Li, "Quasicrystal photonic metasurfaces for radiation controlling of second harmonic generation," Adv. Mater. **31**, 1901188 (2019).
52. X. Y. Xi and X. H. Sun, Photonic bandgap properties of two dimensional photonic quasicrystals with multiple complex structures," Superlattices Microstruct. **129**, 247 (2019).
53. Z. Guo, B. Yan, and J. Liu, "Straight lined and circular interface states in sunflower-type photonic crystals," J. Opt. **22**, 035002 (2020).
54. H. Zhao, J. Xie, and J. Liu, "An approximate theoretical explanation for super-resolution imaging of two-dimensional photonic quasi-crystal flat lens," Appl. Phys. Express **13**, 022007 (2020).
55. T. Hou, R. Ge, W. Tan, and J. Liu, "One-way rotating state of multi-periodicity frequency bands in circular photonic crystal," J. Phys. D **53**, 075104 (2020).
56. W. Jin, M. Song, X. Yue, and Y. Gao, "Optical induced area-controllable two-dimensional eight-fold symmetric photonic quasicrystal microstructures," Opt. Mater. **100**, 109719 (2020).
57. A. D. Sinelnik, I. I. Shishkin, X. Yu, K. B. Samusev, P. A. Belov, M. F. Limonov, P. Ginzburg, and M. V. Rybin, "Experimental Observation of intrinsic light localization in photonic icosahedral quasicrystals," Adv. Opt. Mater. **8**, 2001170 (2020).
58. T. Liu, H. Guo, Y. Pu, and S. Longhi, "Generalized Aubry-André self-duality and mobility edges in non-Hermitian quasiperiodic lattices," Phys. Rev. B **102**, 024205 (2020).
59. C.-B. Hua, R. Chen, B. Zhou, and D.-H. Xu, "Higher-order topological insulator in a dodecagonal quasicrystal," Phys. Rev. B **102**, 241102(R) (2020).
60. S. Biasco, H. E. Beere, D. A. Ritchie, L. Li, and A. G. Davies, E. H. Linfield, and M. S. Vitiello, "Frequency-tunable continuous-wave random lasers at terahertz frequencies," Light Sci. Appl. **8**, 43 (2019).
61. H. Yao, T. Giamarchi, and L. Sanchez-Palencia, "Lieb-Liniger bosons in a shallow quasiperiodic potential: bose glass phase and fractal mott lobes," Phys. Rev. Lett. **125**, 060401 (2020).
62. A. Ramakrishnan, K. K. Kesavan, S. Chavhan, M. R. Nagar, J.-H. Jou, S.-W. Chen, H.-W. Hsiao, J.-M. Zuo, and L. Y. Hung, "Liquid exfoliation of decagonal quasicrystals and its light out-coupling performance in organic light-emitting devices," Adv. Photonics Res. **1**, 2000042 (2020).
63. R. Gautier, H. Yao, and L. Sanchez-Palencia, "Strongly interacting bosons in a two-dimensional quasicrystal lattice," Phys. Rev. Lett. **126**, 110401 (2021).
64. T. M. Mercier, T. Rahman, C. Krishnan, E. Khorani, P. J. Shaw, M. E. Pollard, S. A. Boden, P. G. Lagoudakis, and M. D. B. Charlton, "High symmetry nanophotonic quasi-crystals providing novel light management in silicon solar cells," Nano Energy **84**, 105874 (2021).
65. J. C. Knight, "Photonic crystal fibres," Nature **424**, 847 (2003).
66. P. Russell, "Photonic crystal fibers," Science **299**, 358 (2003).
67. J. C. Knight, T. A. Birks, P. St.J. Russell, and D. M. Atkin, "All-silica single-mode optical fiber with photonic crystal cladding: errata," Opt. Lett. **22**, 484 (1997).
68. S. Kim, C.-S. Kee, and J. Lee, "Novel optical properties of six-fold symmetric photonic quasicrystal fibers," Opt. Express **15**, 13221 (2007).
69. S. Kim and C.-S. Kee, "Dispersion properties of dual-core photonic-quasicrystal fiber," Opt. Express **17**, 15885 (2009).
70. H. Zhao, R. P. Zaccaria, P. Verma, J. Song, and H. Sun, "Validity of the $V$ parameter for photonic quasi-crystal fibers," Opt. Lett. **35**, 1064 (2010).
71. W. Cai, E. Liu, B. Feng, W. Xiao, H. Liu, Z. Wang, S. Wang, T. Liang, J. Liu, and J. Liu, "Dodecagonal photonic quasi-crystal fiber with high birefringence," J. Opt. Soc. Am. A **33**, 2108 (2016).
72. X. Sun and D. J. J. Hu, "Air guiding with photonic quasi-crystal fiber," IEEE Photon. Technol. Lett. **22**, 607 (2010).
73. S. Sivabalan and J. P. Raina, "High normal dispersion and large mode area photonic quasi-crystal fiber stretcher," IEEE Photon. Technol. Lett. **23**, 1139 (2011).
74. F. Sircilli, M. A. R. Franco, and V. A. Serrão, "Dispersion properties of microstructured optical fiber with 12-fold quasicrystal lattice of holes," in

*EUROCON 2007 - The International Conference on "Computer as a Tool"* (2007), p. 1263.
75. S. Sivabalan and J. P. Raina, "Large pitch photonic quasi-crystal fiber amplifier," IEEE Photon. J. **4**, 943 (2012).
76. W. Su, S. Lou, H. Zou, and B. Han, "Design of a highly nonlinear twin bow-tie polymer photonic quasi-crystal fiber with high birefringence," Infrared Phys. Technol. **63**, 62 (2014).
77. S. Matloub, S. M. Hosseini, and A. Rostami, "Analysis and optimization of a dual-core dispersion compensation fiber based on a 12-fold photonic quasi-crystal structure," Appl. Opt. **53**, 8366 (2014).
78. W. Su, S. Lou, H. Zou, and B. Han, "A highly nonlinear photonic quasi-crystal fiber with low confinement loss and flattened dispersion," Opt. Fiber Technol. **20**, 473 (2014).
79. V. Ferrando, Á. Coves, P. Ándres, and J. A. Monsoriu, "Guiding properties of a photonic quasi-crystal fiber based on the Thue-Morse sequence," IEEE Photon. Technol. Lett. **27**, 1903 (2015).
80. M. S. Aruna Gandhi, S. Sivabalan, P. Ramesh Babu, K. Nakkeeran, and K. Senthilnathan, "Design of a photonic quasi-crystal fiber for the generation of few cycle laser pulses," Infrared Phys. Technol. **68**, 69 (2015).
81. M. S. A. Gandhi, S. Sivabalan, P. R. Babu, and K. Senthilnathan, "Designing a biosensor using a photonic quasi-crystal fiber," IEEE Sens. J. **16**, 2425 (2016).
82. M. Valliammai and S. Sivabalan, "Wide-band supercontinuum generation in mid-IR using polarization maintaining chalcogenide photonic quasi-crystal fiber," Appl. Opt. **56**, 4797 (2017).
83. T. Zhao, Z. Lian, T. Benson, X. Wang, W. Zhang, and S. Lou, "Highly-nonlinear polarization-maintaining $As_2Se_3$-based photonic quasi-crystal fiber for supercontinuum generation," Opt. Mater. **73**, 343 (2017).
84. S. Chu, K. Nakkeeran, A. M. Abobaker, S. S. Aphale, P. R. Babu, and K. Senthilnathan, "Design and analysis of surface-plasmon-resonance-based photonic quasi-crystal fiber biosensor for high-refractive-index liquid analytes," IEEE J. Sel. Top. Quantum Electron. **25**, 6900309 (2019).
85. E. Liu, B. Yan, W. Tan, J. Xie, R. Ge, and J. Liu, "Guiding characteristics of sunflower-type fiber," Superlattices Microstruct. **115**, 123 (2018).
86. E. Liu, W. Tan, B. Yan, J. Xie, R. Ge, and J. Liu, "Broadband ultra-flattened dispersion, ultra-low confinement loss and large effective mode area in an octagonal photonic quasi-crystal fiber," J. Opt. Soc. Am. A **35**, 431 (2018).
87. B. Yan, A. Wang, E. Liu, W. Tan, J. Xie, R. Ge, and J. Liu, "Polarization filtering in the visible wavelength range using surface plasmon resonance and a sunflower-type photonic quasi-crystal fiber," J. Phys. D **51**, 155105 (2018).
88. A. Tandjè, J. Yammine, M. Dossou, G. Bouwmans, K. Baudelle, A. Vianou, E. R. Andresen, and L. Bigot, "Ring-core photonic crystal fiber for propagation of OAM modes," Opt. Lett. **44**, 1611 (2019).
89. Q. Liu, B. Yan, and J. Liu, "U-shaped photonic quasi-crystal fiber sensor with high sensitivity based on surface plasmon resonance," Appl. Phys. Express **12**, 052014 (2019).
90. C. Li, B. Yan, and J. Liu, "Refractive index sensing characteristics in a D-shaped photonic quasi-crystal fiber sensor based on surface plasmon resonance," J. Opt. Soc. Am. A **36**, 1663 (2019).
91. J. Han, E. Liu, and J. Liu, "Circular gradient-diameter photonic crystal fiber with large mode area and low bending loss," J. Opt. Soc. Am. A **36**, 533 (2019).
92. E. Liu, S. Liang, and J. Liu, "Double-cladding structure dependence of guiding characteristics in six-fold symmetric photonic quasi-crystal fiber," Superlattices Microstruct. **130**, 61 (2019).
93. M. F. Azman, W. R. Wong, Mhd. H. Mhd. Abd. Cader, R. A. Aoni, G. A. Mahdiraji, and F. R. Mahamd Adikan, "Twin-core sunflower-type photonic quasicrystal fibers incorporated gold, silver, and copper microwire: an ultrashort and broad bandwidth polarization splitter," Opt. Quantum Electron. **51**, 164 (2019).
94. Z. Huo, E. Liu, and J. Liu, "Hollow-core photonic quasicrystal fiber with high birefringence and ultra-low nonlinearity," Chin. Opt. Lett. **18**, 030603 (2020).
95. E. Liu, W. Tan, B. Yan, J. Xie, R. Ge, and J. Liu, "Robust transmission of orbital angular momentum mode based on a dual-cladding photonic quasi-crystal fiber," J. Phys. D **52**, 325110 (2019).
96. Q. Liu, Y. Jiang, C.-J. Hu, W.-S. Lu, Y.-D. Sun, C. Liu, J.-W. Lv, J. Zhao, S.-N. Tai, Z. Yi, and P. K. Chu, "High-sensitivity surface plasmon resonance sensor based on the ten-fold eccentric core quasi-D-shaped photonic quasi-crystal fiber coated with indium tin oxide," Chin. Opt. **15**, 101 (2022).
97. M. Kim and S. Kim, "Photonic quasi-crystal fiber for orbital angular momentum modes with ultra-flat dispersion," Curr. Opt. Photonics **3**, 298 (2019).
98. W. Wei, Z.-M. Zhang, L.-Q. Tang, L. Ding, W.-D. Fan, and Y.-G. Li, "Transmission characteristics of vortex beams in a sixfold photonic quasi-crystal fiber," Acta Phys. Sin. **68**, 114209 (2019).
99. J. P. da Silva and E. R. M. Dantas, "Modal analysis of a photonic quasicrystal fiber doped with germanium," in *SBMO/IEEE MTT-S International Microwave & Optoelectronics Conference (IMOC)* (2013), p. 1.
100. N. A. Mortensen, J. R. Folkenberg, M. D. Nielsen, and K. P. Hansen, "Modal cutoff and the *V* parameter in photonic crystal fibers," Opt. Lett. **28**, 1879 (2003).
101. F. Poli, M. Foroni, M. Bottacini, M. Fuochi, N. Burani, L. Rosa, A. Cucinotta, and S. Selleri, "Single-mode regime of square-lattice photonic crystal fibers," J. Opt. Soc. Am. A **22**, 1655 (2005).
102. H. Zhao, R. Proietti Zaccaria, P. Verma, J. Song, and H. Sun, "Single-mode operation regime for 12-fold index-guiding quasicrystal optical fibers," Appl. Phys. B Lasers Opt. **100**, 499 (2010).
103. W. J. Wadsworth, R. M. Percival, G. Bouwmans, J. C. Knight, T. A. Birks, T. D. Hedley, and P. St.J. Russell, "Very high numerical aperture fibers," IEEE Photon. Technol. Lett. **16**, 843 (2004).
104. B. K. Paul, S. Chakma, M. A. Khalek, and K. Ahmed, "Silicon nano crystal filled ellipse core based quasi photonic crystal fiber with birefringence and very high nonlinearity," Chin. J. Phys. **56**, 2782 (2018).
105. B. K. Paul, K. Ahmed, V. Dhasarathan, and T. K. Nguyen, "Oligoporous-core quasi cladding photonic crystal fiber based micro-sensor for alcohol detection," Phys. B Condens. Matter **584**, 412104 (2020).
106. Y. M. Wang, W. R. Xue, and W. M. Zhang, "Dispersion properties of photonic quasicrystal fiber with an air hole varying cladding," Act. Sin. Quant. Opt. **29**, 1644 (2009).
107. Y. M. Wang, W. R. Xue, and W. M. Zhang, "Dispersion properties of modified octagon photonic quasicrystal fiber," Act. Opt. Sin. **15**, 58 (2009).
108. Z. Q. Li, L. Y. Niu, C. L. Bai, R. Hao, and X. Zhang, "Dispersion property of photonic quasicrystal fibers," Chin. J. Lumin. **34**, 494 (2013).
109. Y. S. Lee, C. G. Lee, and S. Kim, "Annular core photonic quasi-crystal fiber with wideband nearly zero ultra-flat dispersion, low confinement loss and high nonlinearity," Optik **157**, 141 (2018).
110. Y. H. Li, W. De Fan, and Q. Q. Sheng, "A novel photonic quasicrystal fiber with broadband large negative dispersion," Chin. Phys. Lett. **27**, 114211 (2010).
111. S. Rajalingam and Z. C. Alex, "Five-fold symmetric photonic quasi-crystal fiber with high negative dispersion," Res. J. Appl. Sci. Eng. Technol. **9**, 786 (2015).
112. L.-G. Li, L.-S. Yan, G.-Y. Feng, W. Pan, B. Luo, A. Yi, and R.-L. Zhu, "Distortionless large-ratio stretcher for ultra-short pulses using photonic crystal fiber," Opt. Express **18**, 12341 (2010).
113. W. Su, S. Lou, H. Zou, and B. Han, "Highly birefringent ZBLAN photonic quasi-crystal fiber with four circular air holes in the core," Infrared Phys. Technol. **66**, 97 (2014).
114. H. Liu, W. Xiao, W. Cai, E. Liu, B. Feng, Z. Wang, T. Liang, S. Wang, and J. Liu, "Photonic quasi-crystal fiber with high birefringence," Opt. Eng. **55**, 036101 (2016).
115. W. Su, S.-Q. Lou, H. Zou, and B. L. Han, "Highly birefringent $ZrF_4$-$BaF_2$-$LaF_3$-$AlF_3$-NaF photonic quasi-crystal fiber with twin grapefruits holes," Acta Phys. Sin. **63**, 144202 (2014).
116. W.-Y. Liao, W.-D. Fan, Y. Li, J. Chen, F.-H. Bu, H.-P. Li, X.-Y. Wang, and D.-M. Huang, "Investigation of a novel all-solid large-mode-area photonic quasi-crystal fiber," Acta Phys. Sin. **63**, 034206 (2014).
117. S. Maheswaran, B. K. Paul, M. A. Khalek, S. Chakma, K. Ahmed, and M. S. Mani Rajan, "Design of tellurite glass based quasi photonic crystal fiber with high nonlinearity," Optik **181**, 185 (2019).
118. B. K. Paul, M. Abdul Khalek, S. Chakma, and K. Ahmed, "Chalcogenide embedded quasi photonic crystal fiber for nonlinear optical applications," Ceram. Int. **44**, 18955 (2018).
119. I. S. Amiri, M. A. Khalek, S. Chakma, B. K. Paul, K. Ahmed, V. Dhasarathan, and M. S. Mani Rajan, "Design of $Ge_{20}Sb_{15}Se_{65}$ embedded rectangular slotted quasi photonic crystal fiber for higher nonlinearity applications," Optik **184**, 63 (2019).

120. H. Zhang, W. Zhang, L. Xi, X. Tang, X. Zhang, and X. Zhang, "A new type circular photonic crystal fiber for orbital angular momentum mode transmission," IEEE Photon. Technol. Lett. **28**, 1426 (2016).
121. Z.-A. Hu, Y.-Q. Huang, A.-P. Luo, H. Cui, Z.-C. Luo, and W.-C. Xu, "Photonic crystal fiber for supporting 26 orbital angular momentum modes," Opt. Express **24**, 17285 (2016).
122. E. Liu, B. Yan, J. Xie, Y. Peng, F. Gao, and J. Liu, "Dispersion compensation for orbital angular momentum mode based on circular photonic crystal fiber," J. Phys. D. Appl. Phys. **54**, 435104 (2021).
123. A. Rjeb, H. Fathallah, S. Chebaane, and M. Machhout, "Design of novel circular lattice photonic crystal fiber suitable for transporting 48 OAM modes," Optoelectron. Lett. **17**, 501 (2021).
124. Q. Liu, S. Tai, W. Lu, J. Sun, T. Lv, C. Liu, Y. Sun, J. Lv, W. Liu, and T. Sun, "Design of pure silica-based photonic crystal fiber for supporting 114 OAM modes transmission," J. Opt. **23**, 095701 (2021).
125. T. Wu, Y. Shao, Y. Wang, S. Cao, W. Cao, F. Zhang, C. Liao, J. He, Y. Huang, M. Hou, and Y. Wang, "Surface plasmon resonance biosensor based on gold-coated side-polished hexagonal structure photonic crystal fiber," Opt. Express **25**, 20313 (2017).
126. S. Revathi, S. R. Inabathini, and J. Pal, "Pressure and temperature sensor based on a dual core photonicquasi-crystal fiber," Optik **126**, 3395 (2015).
127. M. S. Aruna Gandhi, Y. Zhao, H. Y. Fu, and Q. Li, "A highly versatile porous core photonic quasicrystal fiber based refractive index terahertz sensor," Sensors **22**, 3469 (2022).
128. Q. Liu, J. Sun, Y. Sun, Z. Ren, C. Liu, J. Lv, F. Wang, L. Wang, W. Liu, T. Sun, and P. K. Chu, "Surface plasmon resonance sensor based on photonic crystal fiber with indium tin oxide film," Opt. Mater. **102**, 109800 (2020).
129. Y. Sun, H. Mu, J. Sun, Q. Liu, C. Liu, W. Liu, J. Zhao, J. Lv, T. Sun, and P. K. Chu, "Investigation of a high-sensitivity surface plasmon resonance sensor based on the eccentric core quasi D-shape photonic quasi-crystal fiber," J. Mod. Opt. **68**, 555 (2021).
130. Q. Liu, J. Zhao, Y. Sun, W. Liu, C. Liu, J. Lv, T. Lv, Y. Jiang, B. Li, F. Wang, T. Sun, and P. K. Chu, "High-sensitivity methane sensor composed of photonic quasi-crystal fiber based on surface plasmon resonance," J. Opt. Soc. Am. A **38**, 1438 (2021).
131. E. Liu, B. Yan, H. Zhou, Y. Liu, G. Liu, and J. Liu, "OAM mode-excited surface plasmon resonance for refractive index sensing based on a photonic quasi-crystal fiber," J. Opt. Soc. Am. B **38**, F16 (2021).
132. A. Medjouri, L. M. Simohamed, O. Ziane, A. Boudrioua, and Z. Becer, "Design of a circular photonic crystal fiber with flattened chromatic dispersion using a defected core and selectively reduced air holes: application to supercontinuum generation at 1.55 μm," Photonics Nanostructures-Fundam. Appl. **16**, 43 (2015).
133. G. Dhanu Krishna, G. Prasannan, S. K. Sudheer, and V. P. Mahadevan Pillai, "Analysis of zero dispersion shift and supercontinuum generation at near IR in circular photonic crystal fibers," Optik **145**, 599 (2017).
134. R. Ahmad, M. Komanec, and S. Zvanovec, "Circular lattice photonic crystal fiber for mid-IR supercontinuum generation," IEEE Photon. Technol. Lett. **28**, 2736 (2016).
135. A. Medjouri and D. Abed, "Mid-infrared broadband ultraflat-top supercontinuum generation in dispersion engineered Ge-Sb-Se chalcogenide photonic crystal fiber," Opt. Mater. **97**, 109391 (2019).
136. P. Zhang, J. Zhang, P. Yang, S. Dai, X. Wang, and W. Zhang, "Fabrication of chalcogenide glass photonic crystal fibers with mechanical drilling," Opt. Fiber Technol. **26**, 176 (2015).
137. V. V. R. K. Kumar, A. K. George, W. H. Reeves, J. C. Knight, P. St.J. Russell, F. G. Omenetto, and A. J. Taylor, "Extruded soft glass photonic crystal fiber for ultrabroad supercontinuum generation," Opt. Express **10**, 1520 (2002).
138. J. Livage, "Sol-gel processes," Curr. Opin. Solid State Mater. Sci. **2**, 132 (1997).
139. R. T. Bise and D. J. Trevor, "Sol-gel derived microstructured fiber: fabrication and characterization," in *Optical Fiber Communication Conference* (2005), paper OWL6.
140. H. El Hamzaoui, Y. Ouerdane, L. Bigot, G. Bouwmans, B. Capoen, A. Boukenter, S. Girard, and M. Bouazaoui, "Sol-gel derived ionic copper-doped microstructured optical fiber: a potential selective ultraviolet radiation dosimeter," Opt. Express **20**, 29751 (2012).
141. A. Bertoncini and C. Liberale, "3D printed waveguides based on photonic crystal fiber designs for complex fiber-end photonic devices," Optica **7**, 1487 (2020).
142. Y. Wen, I. Chremmos, Y. Chen, G. Zhu, J. Zhang, J. Zhu, Y. Zhang, J. Liu, and S. Yu, "Compact and high-performance vortex mode sorter for multi-dimensional multiplexed fiber communication systems," Optica **7**, 254 (2020).
143. M. C. Rechtsman, J. M. Zeuner, Y. Plotnik, Y. Lumer, D. Podolsky, F. Dreisow, S. Nolte, M. Segev, and A. Szameit, "Photonic Floquet topological insulators," Nature **496**, 196 (2013).
144. D. Leykam, M. C. Rechtsman, and Y. D. Chong, "Anomalous topological phases and unpaired Dirac cones in photonic Floquet topological insulators," Phys. Rev. Lett. **117**, 013902 (2016).
145. Z. Yang, E. Lustig, Y. Lumer, and M. Segev, "Photonic Floquet topological insulators in a fractal lattice," Light Sci. Appl. **9**, 128 (2020).
146. M. A. Bandres, M. C. Rechtsman, and M. Segev, "Topological photonic quasicrystals: fractal topological spectrum and protected transport," Phys. Rev. X **6**, 011016 (2016).
147. M. Verbin, O. Zilberberg, Y. Lahini, Y. E. Kraus, and Y. Silberberg, "Topological pumping over a photonic Fibonacci quasicrystal," Phys. Rev. B **91**, 064201 (2015).
148. Z. Che, Y. Zhang, W. Liu, M. Zhao, J. Wang, W. Zhang, F. Guan, X. Liu, W. Liu, L. Shi, and J. Zi, "Polarization singularities of photonic quasicrystals in momentum space," Phys. Rev. Lett. **127**, 043901 (2021).
149. R. Gong, M. Zhang, H. Li, and Z. Lan, "Topological photonic crystal fibers based on second-order corner modes," Opt. Lett. **46**, 3849 (2021).
150. Y. Liu, A. Zhou, and L. Yuan, "Multi-functional fiber-optic sensor based on helix structure and fiber Bragg gratings for shape sensing," Opt. Laser Technol. **143**, 107327 (2021).
151. J. Yang, W. Li, H. Zhang, X. Zhang, L. Xi, and W. Zhang, "Modeling of the twist-induced effect in circular photonic crystal fiber transmitting orbital angular momentum modes," Results Phys. **28**, 104626 (2021).
152. G. K. L. Wong, M. S. Kang, H. W. Lee, F. Biancalana, C. Conti, T. Weiss, and P. St.J. Russell, "Excitation of orbital angular momentum resonances in helically twisted photonic crystal fiber," Science **337**, 446 (2012).
153. X. Xi, G. K. L. Wong, T. Weiss, and P. St.J. Russell, "Measuring mechanical strain and twist using helical photonic crystal fiber," Opt. Lett. **38**, 5401 (2013).
154. H. Wang and A. Yang, "Dispersion and loss control of high birefringence photonic crystal fiber with CdSe/ZnS quantum dot film," J. Opt. **19**, 045803 (2017).
155. J. Yang, I. Ghimire, P. C. Wu, S. Gurung, C. Arndt, D. P. Tsai, and H. W. H. Lee, "Photonic crystal fiber metalens," Nanophotonics **8**, 443 (2019).